Meccanica
https://doi.org/10.1007/s11012-025-01959-7

RESEARCH

On the myocardium modeling under multimodal deformations: a comparison between costa's, Holzapfel and Ogden's formulations

Nicolás Laita · Miguel Ángel Martínez · Manuel Doblaré · Estefanía Peña

Received: 15 October 2024 / Accepted: 18 February 2025

Abstract In this study we evaluate the performance of different constitutive biomechanical models, focusing on their ability to reproduce the mechanical behavior of myocardial tissue under various deformation modes. Three constitutive models were analyzed assuming incompressible formulations: the invariant-based formulation of the Costa model, the Holzapfel–Ogden (HO) model, and its extended version (HOE). The study aimed to identify which model provides the best fit for different experimental data, including equibiaxial (EBx), true biaxial (TBx), simple triaxial shear (STS), and combined data sets (Equibiaxial + Shear, True biaxial + Shear). The results showed that the Costa model generally performed better when considering combined datasets, providing a good balance between fitting accuracy and parameter stability, while using the least number of parameters among the contrasted models. The HO model demonstrated reasonable fitting abilities but struggled with non-equibiaxial conditions and clearly orthotropic simple shear datasets. The extended HOE model improved the fitting performance of the standard HO formulation for more complex data, particularly in shear tests, but introduced additional complexity and a higher number of parameters. Therefore, our study highlights the importance of analyzing which validated constitutive formulation is able to adapt to the available experimental data, especially when mixed deformation modes are involved. While all the three models tested performed adequately, the Costa model proved to be the most versatile, especially when dealing with various experimental conditions, providing insights for future research on biomechanical modeling of cardiac tissue.

Keywords Cardiovascular mechanics · Constitutive modeling · Experimental fitting · Multimodal deformation analysis

N. Laita · M. Á. Martínez · M. Doblaré (✉) · E. Peña
Aragon Institute of Engineering Research (I3A), University of Zaragoza, Zaragoza, Spain
e-mail: mdoblare@unizar.es

N. Laita
e-mail: nlaita@unizar.es

M. Á. Martínez
e-mail: miguelam@unizar.es

E. Peña
e-mail: fany@unizar.es

M. Á. Martínez · M. Doblaré · E. Peña
Biomedical Research Networking Center in Bioengineering, Biomaterials and Nanomedicine (CIBER-BBN), Madrid - Madrid, Spain

M. Doblaré
Aragon Institute of Health Research (IIS Aragon), Zaragoza, Spain

M. Doblaré
Nanjing Tech University, Nanjing, China

Published online: 12 April 2025

1 Introduction

The passive mechanical response of the myocardium has been a significant focus of study over the past decades due to its critical role in cardiac functionality [1, 2]. Consequently, numerous studies have been dedicated to the experimental characterization of its mechanical properties and the development of mathematical models capable of reproducing cardiac physiology.

Several experimental protocols have been followed over the last decades. A prevalent approach is the analysis of biopsied cardiac tissue samples under pure deformation modes, aiming to preserve the tissue as closely as possible to physiological conditions, referred to as *in vitro* testing. Early studies focused on uniaxial tests [3], but they were immediately followed by planar equibiaxial tests (EBx) [4–6], to assess tissue anisotropy, and true biaxial characterization (TBx) [7–13], to assess direction-dependent and cross-coupling effects. Later on, simple triaxial shear tests (STS) [14, 15] were introduced, to assess tissue orthotropy, as well as combinations of simple shear and true biaxial tests [16, 17] or even simple and pure triaxial shear testing [18, 19]. Apart from this *in vitro* characterization, several studies have focused on deriving *in vivo* properties from medical imaging [20–25].

In terms of constitutive modeling, the myocardium has consistently been described as a hyperelastic nonlinear material, considering several assumptions of anisotropy, consistent with its fibrous structure. Thus, several Strain Energy Density Functions (SEDFs) have been proposed. Early heart models assumed isotropic formulations [26, 27]. Subsequently, transversely isotropic formulations [5, 27–31] emerged as the first to incorporate the anisotropic nature of the myocardium, although simplified by distinguishing only the direction of the myocyte fibers. However, it is well-known that myocardium presents a layered distribution of parallel myocyte 'sheets' separated by extensive cleavage planes [32], defining three principal mechanical directions: the muscular fiber direction (F), the fiber-sheet direction (S), and the normal-to-fiber-sheet (N) direction. Hence, orthotropic models (considering different behaviors along the F-S-N axes) were introduced [33–37], being the one by Holzapfel & Ogden (HO) [37] and by Costa et al. [36] two of the most used . For a more comprehensive review, the reader is referred to [38].

The selection of a specific constitutive model is highly influenced by the type of input data considered. Studies based on *in vivo* data often use transversely isotropic formulations [20–25], as the limited *in vivo* experimental data does not allow for a straightforward orthotropic characterization. Regarding *in vitro* experimental data, comparative studies by Schmid et al. [34, 35] focused on evaluating which models best reproduce the simple shear data obtained in [14] using various criteria, such as goodness of fit, determinability, and variability. They noticed relevant differences between the evaluated models, although most of them produced an adequate response. Later studies by Avazmohammadi et al. [18] and Li et al. [19] also analyzed the performance of the HO model [37] against a set of simple and pure shear data using different metrics, observing that extending the traditional HO formulation was necessary to achieve a better fit. Nordsletten et al. [39] conducted a comparison between Costa's and Holzapfel & Ogden's formulations and concluded that Costa's has superior predictive capabilities when applied to non-equibiaxial biaxial stretching, but the HO model has better predictive ability for highly nonlinear responses. Finally, in a previous study [40], we also compared the fitting and predictive capabilities of the Costa, HO, and extended HO models using a set of true biaxial and shear data, observing a good response in all models, though slightly superior for Costa's.

However, in most *in vitro* data-based studies, the analysis of which model best suits their specific dataset is often overlooked, being the most common practice to directly selecting one of the most frequently used models. Furthermore, few studies have thoroughly analyzed the response of various models to different types of experimental data. The most notable work in this regard is probably the one by Schmid et al. [34, 35]. However, these studies are relatively outdated and do not include some of the models most widely used today. Besides, they only evaluate the models' response to the STS dataset presented by Dokos et al. [14]. The studies by Avazmohammadi et al. [18, 19] continued this line of research by extending the analysis to the HO model and even considering an extended formulation of such HO model (HOE). Nevertheless, they focused only on HO-derived formulations and were limited to simple and pure shear modes.

In this study, we analyze the most common orthotropic formulations available nowadays, specifically those of Costa and HO, as well as the HOE formulation presented in [19]. Our goal is to evaluate how each of these models performs for different types of experimental data, using the most common *in vitro* testing methodologies found in the literature. To achieve this, we considered five sets of data, including exclusively equibiaxial tests, true biaxial tests, simple shear tests, and two different combined datasets (equibiaxial + simple shear and true biaxial + simple shear). We aim to determine which constitutive law is more suitable for these different experimental datasets and to assess whether the model selection should be adapted based on the available experimental data. To the best of our knowledge, no previous study has conducted such a comprehensive analysis of the response of different constitutive models to a variety of experimental data. We hope this work will guide future research in selecting the most appropriate material model for a specific study.

2 Myocardium constitutive model

We consider the myocardial tissue as orthotropic, hyperelastic, and incompressible. To ensure an accurate reproduction of the experimental behavior, two widely used material models have been contrasted, the invariant-based version of the Costa model [36] and the Holzapfel & Ogden (HO) model [37]. Following classic notation, we define the deformation of a certain body as the motion of its points from their reference configuration, $\Omega_0 \subset \mathbb{R}^3$, to their current-state positions, $\Omega_t \subset \mathbb{R}^3$. Hence, we define the relative motion of any point in the reference domain, $\mathbf{X} \in \Omega_0$, by its current coordinates $\mathbf{x}(\mathbf{X}, t)$. The deformation gradient is then defined as $\mathbf{F} = \nabla_x \mathbf{x}$, being its determinant the Jacobian. of the deformation, $J = det(\mathbf{F}) > 0$ ($J = 1$ for incompressible materials). Finally, we consider the strain being described by the right Cauchy Green tensor, $\mathbf{C} = \mathbf{F}^T\mathbf{F}$. The stress–strain relationship in a hyperelastic material is given by the strain energy density function (SEDF), Ψ, representing the stored elastic energy per unit volume. Here, the SEDF will be expressed as a function of the invariants of $\mathbf{C}$, defined as

$$I_1 = \mathbf{C} : \mathbf{I}, \quad I_2 = det(\mathbf{C})\mathbf{C}^{-1} : \mathbf{I}, \quad I_3 = det(\mathbf{C}) = J. \tag{1}$$

For an orthotropic material such as the myocardium, additional anisotropic pseudo-invariants along the microstructural directions (fiber-sheet-normal axes) are commonly used. These pseudo-invariants represent the squared stretch along these directions:

$$I_{ff} = \mathbf{C} : \mathbf{e}_f \otimes \mathbf{e}_f, \quad I_{ss} = \mathbf{C} : \mathbf{e}_s \otimes \mathbf{e}_s, \quad I_{nn} = \mathbf{C} : \mathbf{e}_n \otimes \mathbf{e}_n, \tag{2}$$

where $\mathbf{e}_k$ ($k \in \{f, s, n\}$) denote the unitary vectors in each direction. Likewise, the coupling pseudo-invariants between the microstructural directions, which measure the deviation from orthogonality of the fibers under strain and have no role in volumetric deformations are expressed as

$$I_{fs} = \mathbf{C} : \mathbf{e}_f \otimes \mathbf{e}_s, \quad I_{fn} = \mathbf{C} : \mathbf{e}_f \otimes \mathbf{e}_n, \quad I_{sn} = \mathbf{C} : \mathbf{e}_s \otimes \mathbf{e}_n. \tag{3}$$

Costa's model [36] considers an orthotropic formulation of the exponential Fung-type and is normally formulated in terms of the rotated Green Lagrange strain tensor. However, as presented by Nordsletten et al. [39], we can also obtain a right Cauchy Green strain tensor invariants-based formulation, which will be referred to here as Costa model

$$\begin{aligned} \Psi &= \frac{C}{4}[exp(Q(\mathbf{C})) - 1] + p(J-1), \\ Q(\mathbf{C}) &= \sum_{kl \in R_{Costa}} b_{kl}(I_{kl} - \delta_{kl})^2, \end{aligned} \tag{4}$$

where $R_{Costa} = [ff, ss, nn, fs, fn, sn]$ and δ_{kl} denotes the Kronecker delta. The Costa model thus depends on a total of 7 parameters, an external scaling constant, C, and 6 anisotropy parameters, b_{kl}. The second Piola Kirchhoff stress tensor can be obtained from its expression in terms of the invariants as

$$\mathbf{S} = \sum_{kl \in R} 2\frac{\partial \Psi}{\partial I_{kl}} sym(\mathbf{e}_k \otimes \mathbf{e}_l) + pJ\mathbf{C}^{-1}, \tag{5}$$

where $sym(\mathbf{X}) = \frac{1}{2}(\mathbf{X} + \mathbf{X}^T)$ represents the symmetric part of a given tensor. Finally, the first Piola Kirchhoff (PK1) and Cauchy stress tensors can be obtained through the standard weighted push forward operations ($\mathbf{P} = J^{-1}\mathbf{F}\mathbf{S}$ and $\boldsymbol{\sigma} = J^{-1}\mathbf{F}\mathbf{S}\mathbf{F}^T$, respectively). For the HO model, the SDEF is characterized by the following expression

$$\Psi(\mathbf{C}) = \Psi_{iso}(I_1) + \sum_{kl \in R_{HO}} \Psi_{kl}(I_{kl}) + p(J-1), \tag{6}$$

where $R_{HO} = [ff, ss, fs]$ and

$$\Psi_{iso}(I_1) = \frac{a}{2b}[exp(b(I_1 - 3)) - 1], \tag{7}$$

$$I_{kl} = \frac{a_{kl}}{2b_{kl}}[exp(b_{kl}(I_{kl} - \delta_{kl})^2) - 1]. \tag{8}$$

The HO model thus depends on a total of 8 parameters. Analogously to Eq. (5), the second Piola-Kirchhoff stress tensor is given by

$$\mathbf{S} = 2\frac{\partial \Psi_{iso}}{\partial I_1}\mathbf{I} + \sum_{kl \in R_{HO}} 2\frac{\partial \Psi_{kl}}{\partial I_{kl}} sym(\mathbf{e}_k \otimes \mathbf{e}_l) + pJ\mathbf{C}^{-1}. \tag{9}$$

Both the Costa and HO models have similar formulations, presenting both pros and cons for parameter estimation. The main differences are (i) the Costa model strain-energy terms are coupled in a single exponential function, while the HO SEDF is presented as a sum of different exponentials; (ii) the Costa model also includes *nn*, *fn* and *sn* strain modes and (iii) the HO model includes an isotropic term which represents the stiffness of the extracellular matrix; (iv) HO formulations decouple additively the isotropic and non-isotropic contributions, while Costa does not include an isotropic term. Regarding (ii), Li et al. [19] presented an extended version of the HO model (HOE) which hypothesizes that the myocardium exhibits further modes of coupling besides the ones considered by the I_{fs} and includes the two other I_{kl} pseudo-invariants in Eq. (3). It should be mentioned that these additional terms were originally proposed by Holzapfel and Ogden [37] but they were ultimately excluded. With the addition of these terms Eqs. (10) and (11) result as

$$\Psi(\mathbf{C}) = \Psi_{iso}(I_1) + \sum_{kl \in R_{HOE}} \Psi_{kl}(I_{kl}) + p(J - 1), \tag{10}$$

$$\mathbf{S} = 2\frac{\partial \Psi_{iso}}{\partial I_1}\mathbf{I} + \sum_{kl \in R_{HOE}} 2\frac{\partial \Psi_{kl}}{\partial I_{kl}} sym(\mathbf{e}_k \otimes \mathbf{e}_l) + pJ\mathbf{C}^{-1}, \tag{11}$$

where now $R_{HOE} = [ff, ss, fs, fn, sn]$. Li et al. [19] stated that the inclusion of these additional terms improved the fitting and predictive capability of the HO model when applied to simple and pure shear strains. However, including the additional I_{kl} terms implies a significant increase in the number of material parameters in the SEDF (8 parameters for HO versus 12 parameters for HOE).

3 Experimental characterization of porcine tissue

We compared the three selected constitutive laws against our recent *in vitro* experimental dataset [17]. Briefly, porcine left ventricular biopsy specimens were obtained from 13 white pigs (Sus scrofa domesticus) of 18–22 weeks of age (weight between 55–65 kg). All experiments complied with the regulations of the local animal welfare committee for the care and use of experimental animals and were approved by local authorities (Ethics Committee on Animal Experimentation, CEAEA, of the University of Zaragoza). All animal procedures conformed to the guidelines from Directive 2010/63/EU of the European Parliament on the protection of animals used for scientific purposes. Biaxial and triaxial shear tests were conducted according to the protocols presented in [14, 16]. For biaxial testing, 25×25 mm parallel-to-the-epicardium slices were obtained at different wall thickness levels. Samples were cut alongside the local main-fiber and cross-fiber directions, corresponding to the FN plane according to the LeGrice FSN coordinate system. Five different loading ratios were applied between MFD and CFD (1(CFD):1(MFD), 1:0.75, 1:0.5, 0.75:1, and 0.5:1). For shear testing, 4 mm cubic samples were also aligned with the FSN axis, obtaining 6 different shear modes (FN-FS-SF-SN-NF-NS) [14]. Both tests were performed at various strain levels under quasi-static conditions to neglect viscoelastic effects.

Specifically, we utilized the preconditioned biaxial data at the last applied extension level (20%) and the preconditioned positive shear data at the last extension level (50%). The medial zone was selected as the reference area due to a higher fiber alignment, which can be considered locally homogeneous, compared to the apical zone. This facilitates an objective characterization of the mechanical response following the orthotropic directions of the tissue, which are fundamental to the selected constitutive myocardial models. A more detailed description of the experimental procedures is given in [17], and the complete experimental dataset is available at [41]. Figure 1 summarizes the experimental conditions and main results.

3.1 *In vitro* tests analytical solution

Here we describe the full procedure to obtain the Costa, HO, and HOE constitutive laws analytical solution, both for the selected TBx and STS tests.

3.1.1 Biaxial extension tests

Considering a biaxial extension test in $\mathbf{e}_f$ and $\mathbf{e}_n$ as shown in Fig. 1a, we can define the deformation gradient tensor, $\mathbf{F}$, for an incompressible material as

$$\mathbf{F} = \begin{pmatrix} \lambda_f & 0 & 0 \\ 0 & \lambda_s & 0 \\ 0 & 0 & \lambda_n \end{pmatrix} = \begin{pmatrix} \lambda_f & 0 & 0 \\ 0 & \frac{1}{\lambda_f \lambda_n} & 0 \\ 0 & 0 & \lambda_n \end{pmatrix}, \tag{12}$$

where λ_f, λ_s and λ_n are the respective elongation in the LeGrice directions F, S and N. Then, as described above, we can define the right Cauchy-Green tensor, $\mathbf{C}$, as

$$\mathbf{C} = \begin{pmatrix} \lambda_f^2 & 0 & 0 \\ 0 & \frac{1}{\lambda_f^2 \lambda_n^2} & 0 \\ 0 & 0 & \lambda_n^2 \end{pmatrix}. \tag{13}$$

According to Eq. 5 we can write the PK2 tensor, $\mathbf{S}$, as

$$\begin{aligned} \mathbf{S} &= \begin{pmatrix} 2\frac{\partial \Psi}{\partial I_{ff}} & amp;\frac{\partial \Psi}{\partial I_{fs}} & amp;\frac{\partial \Psi}{\partial I_{fn}} \\ \frac{\partial \Psi}{\partial I_{fs}} & amp;2\frac{\partial \Psi}{\partial I_{ss}} & amp;\frac{\partial \Psi}{\partial I_{sn}} \\ \frac{\partial \Psi}{\partial I_{fn}} & amp;\frac{\partial \Psi}{\partial I_{sn}} & amp;2\frac{\partial \Psi}{\partial I_{nn}} \end{pmatrix} + pJ\mathbf{C}^{-1} \\ &= \begin{pmatrix} 2\frac{\partial \Psi}{\partial I_{ff}} + \frac{p}{\lambda_f^2} & amp;\frac{\partial \Psi}{\partial I_{fs}} & amp;\frac{\partial \Psi}{\partial I_{fn}} \\ \frac{\partial \Psi}{\partial I_{fs}} & amp;2\frac{\partial \Psi}{\partial I_{ss}} + p\lambda_f^2\lambda_n^2 & amp;\frac{\partial \Psi}{\partial I_{sn}} \\ \frac{\partial \Psi}{\partial I_{fn}} & amp;\frac{\partial \Psi}{\partial I_{sn}} & amp;2\frac{\partial \Psi}{\partial I_{nn}} + \frac{p}{\lambda_n^2} \end{pmatrix}. \end{aligned} \tag{14}$$

The Cauchy stress tensor can be obtained by $\boldsymbol{\sigma} = J^{-1}\mathbf{F}\mathbf{S}\mathbf{F}^T$, resulting in

$$\boldsymbol{\sigma} = \begin{pmatrix} 2\lambda_f^2 \cdot \frac{\partial \Psi}{\partial I_{ff}} + p & \frac{1}{\lambda_n} \cdot \frac{\partial \Psi}{\partial I_{fs}} & \lambda_f \lambda_n \cdot \frac{\partial \Psi}{\partial I_{fn}} \\ \frac{1}{\lambda_n} \cdot \frac{\partial \Psi}{\partial I_{fs}} & \frac{2}{\lambda_f^2 \lambda_n^2} \cdot \frac{\partial \Psi}{\partial I_{ss}} + p & \frac{1}{\lambda_f} \cdot \frac{\partial \Psi}{\partial I_{sn}} \\ \lambda_f \lambda_n \cdot \frac{\partial \Psi}{\partial I_{fn}} & \frac{1}{\lambda_f} \cdot \frac{\partial \Psi}{\partial I_{sn}} & 2\lambda_n^2 \cdot \frac{\partial \Psi}{\partial I_{nn}} + p \end{pmatrix}. \tag{15}$$

Then, p is assessed by imposing the stress-free boundary condition $\sigma_{ss} = 0$. The PK1 tensor ($\mathbf{P} = \mathbf{F}\mathbf{S}$) is also determined as it will be implemented at the minimization process. The final expressions for P_{ff} and P_{nn} are

$$P_{ff}^{Costa} = \left[b_{ff}(\lambda_f^2 - 1) - b_{ss} \frac{\left(\frac{1}{\lambda_f^2 \lambda_n^2} - 1 \right)}{\lambda_f^4 \lambda_n^2} \right] C \cdot \lambda_f \cdot e^{Q_{Bx}} \tag{16}$$

$$P_{nn}^{Costa} = \left[b_{nn}(\lambda_n^2 - 1) - b_{ss} \frac{\left(\frac{1}{\lambda_f^2 \lambda_n^2} - 1 \right)}{\lambda_f^2 \lambda_n^4} \right] C \cdot \lambda_n \cdot e^{Q_{Bx}} \tag{17}$$

where

$$e^{Q_{Bx}} = e^{\left(b_{ff}\left(\lambda_f^2 - 1\right)^2 + b_{ss}\left(\frac{1}{\lambda_f^2 \lambda_n^2} - 1 \right)^2 + b_{nn}\left(\lambda_n^2 - 1\right)^2 \right)} \tag{18}$$

Repeating this analytical development for HO, we arrive to:

$$\begin{aligned} P_{ff}^{HO} &= \frac{a}{\lambda_f^3 \lambda_n^2}(\lambda_f^4 \lambda_n^2 - 1) \cdot e^{\left(b\left(\frac{\lambda_f^4 \lambda_n^2 + \lambda_f^2 \lambda_n^4 - 3\lambda_f^2 \lambda_n^2 + 1}{\lambda_f^2 \lambda_n^2} \right)^2 \right)} \\ &\quad + 2a_{ff} \cdot \lambda_f(\lambda_f^2 - 1) \cdot e^{\left(b_{ff}\left(\lambda_f^2 - 1\right)^2 \right)} \\ &\quad + \frac{2a_{ss}}{\lambda_f^5 \lambda_n^4}(\lambda_f^2 \lambda_n^2 - 1) \cdot e^{\left(b_{ss}\left(\frac{1}{\lambda_f^2 \lambda_n^2} - 1 \right)^2 \right)} \end{aligned} \tag{19}$$

$$\begin{aligned} P_{nn}^{HO} &= \frac{a}{\lambda_f^2 \lambda_n^3}(\lambda_f^2 \lambda_n^4 - 1) \cdot e^{\left(b\left(\frac{\lambda_f^4 \lambda_n^2 + \lambda_f^2 \lambda_n^4 - 3\lambda_f^2 \lambda_n^2 + 1}{\lambda_f^2 \lambda_n^2} \right)^2 \right)} \\ &\quad + \frac{2a_{ss}}{\lambda_f^4 \lambda_n^5}(\lambda_f^2 \lambda_n^2 - 1) \cdot e^{\left(b_{ss}\left(\frac{1}{\lambda_f^2 \lambda_n^2} - 1 \right)^2 \right)} \end{aligned} \tag{20}$$

Lastly, since the differences between HO and HOE arise from the inclusion of the coupling pseudo-invariants I_{fn} and I_{sn}, the analytical expressions of P_{ff} and P_{nn} remain unchanged, as they only involve hydrostatic terms. Therefore, $P_{ff}^{HOE} = P_{ff}^{HO}$ and $P_{nn}^{HOE} = P_{nn}^{HO}$.

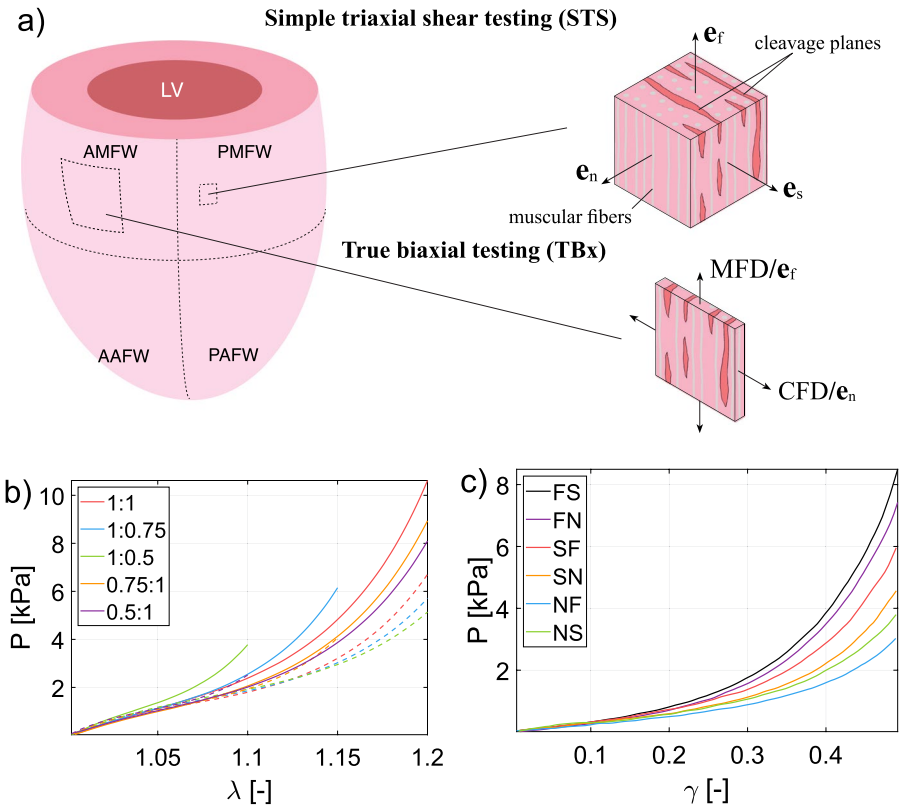

Fig. 1 Considered *in vitro* experiments protocol summary. **a** Scheme of the sample obtention procedure. Biaxial and triaxial shear samples were obtained and aligned with the FSN directions. **b** Considered biaxial extension tests mean results at 20% of deformation. Solid lines correspond to MFD and dotted lines to CFD. Legend ratios are referred to as CFD:MFD. **c** Considered simple triaxial shear results at 50% of shear strain

3.1.2 Simple triaxial shear test

Depending on the shear direction concerning the different tissue's orthotropy orientations, there are a total of 6 different simple shear stress configurations as stated by Dokos et al. [14]. Following the notation presented in [37], we consider as FS mode the shear stress in the FS plane where the loading direction is the S-direction, and so for the resting 5 configurations. Then, considering a sample orientation as displayed in Fig. 1a, we define the deformation gradient, $\mathbf{F}$, for all the shearing configurations as

$$\mathbf{F}_{FS} = \begin{pmatrix} 1 & 0 & 0 \\ \gamma & 1 & 0 \\ 0 & 0 & 1 \end{pmatrix}, \quad \mathbf{F}_{FN} = \begin{pmatrix} 1 & 0 & 0 \\ 0 & 1 & 0 \\ \gamma & 0 & 1 \end{pmatrix}, \quad \mathbf{F}_{SF} = \begin{pmatrix} 1 & \gamma & 0 \\ 0 & 1 & 0 \\ 0 & 0 & 1 \end{pmatrix},$$
$$\mathbf{F}_{SN} = \begin{pmatrix} 1 & 0 & 0 \\ 0 & 1 & 0 \\ 0 & \gamma & 1 \end{pmatrix}, \quad \mathbf{F}_{NF} = \begin{pmatrix} 1 & 0 & \gamma \\ 0 & 1 & 0 \\ 0 & 0 & 1 \end{pmatrix}, \quad \mathbf{F}_{NS} = \begin{pmatrix} 1 & 0 & 0 \\ 0 & 1 & \gamma \\ 0 & 0 & 1 \end{pmatrix}. \tag{21}$$

Analogously to the process described for the biaxial conditions, for the Costa formulation, we reach the following expressions for the PK1 terms for the shear tests

$$P_{fs}^{Costa} = \left(\gamma^2 \cdot b_{ff} + \frac{b_{fs}}{2}\right) \cdot \gamma \cdot C \cdot e^{(b_{ff}\cdot\gamma^4 + b_{fs}\cdot\gamma^2)}. \tag{22}$$

$$P_{fn}^{Costa} = \left(\gamma^2 \cdot b_{ff} + \frac{b_{fn}}{2}\right) \cdot \gamma \cdot C \cdot e^{(b_{ff}\cdot\gamma^4 + b_{fn}\cdot\gamma^2)}. \tag{23}$$

$$P_{sf}^{Costa} = \left(\gamma^2 \cdot b_{ss} + \frac{b_{fs}}{2}\right) \cdot \gamma \cdot C \cdot e^{(b_{ss}\cdot\gamma^4 + b_{fs}\cdot\gamma^2)}, \tag{24}$$

$$P_{sn}^{Costa} = \left(\gamma^2 \cdot b_{ss} + \frac{b_{sn}}{2}\right) \cdot \gamma \cdot C \cdot e^{(b_{ss}\cdot\gamma^4 + b_{sn}\cdot\gamma^2)}, \tag{25}$$

$$P_{nf}^{Costa} = \left(\gamma^2 \cdot b_{nn} + \frac{b_{fn}}{2}\right) \cdot \gamma \cdot C \cdot e^{(b_{nn}\cdot\gamma^4 + b_{fn}\cdot\gamma^2)}, \tag{26}$$

$$P_{ns}^{Costa} = \left(\gamma^2 \cdot b_{nn} + \frac{b_{sn}}{2}\right) \cdot \gamma \cdot C \cdot e^{(b_{nn}\cdot\gamma^4 + b_{sn}\cdot\gamma^2)}, \tag{27}$$

Similarly for the HO model, we obtain:

$$P_{fs}^{HO} = ((\gamma^2+3)-\gamma^2)\frac{a}{3}\cdot\gamma\cdot\exp(b\cdot\gamma^2)+ + 2a_{ff}\cdot\gamma^3\cdot\exp(b_{ff}\cdot\gamma^4)+a_{fs}\cdot\gamma\cdot\exp(b_{fs}\cdot\gamma^2), \quad (28)$$

$$P_{fn}^{HO} = ((\gamma^2+3)-\gamma^2)\frac{a}{3}\cdot\gamma\cdot\exp(b\cdot\gamma^2)+ + 2a_{ff}\cdot\gamma^3\cdot\exp(b_{ff}\cdot\gamma^4), \quad (29)$$

$$P_{sf}^{HO} = ((\gamma^2+3)-\gamma^2)\frac{a}{3}\cdot\gamma\cdot\exp(b\cdot\gamma^2)+ + 2a_{ss}\cdot\gamma^3\cdot\exp(b_{ss}\cdot\gamma^4)+a_{fs}\cdot\gamma\cdot\exp(b_{fs}\cdot\gamma^2), \quad (30)$$

$$P_{sn}^{HO} = ((\gamma^2+3)-\gamma^2)\frac{a}{3}\cdot\gamma\cdot\exp(b\cdot\gamma^2)+ + 2a_{ss}\cdot\gamma^3\cdot\exp(b_{ss}\cdot\gamma^4) \quad (31)$$

$$P_{nf}^{HO} = P_{ns}^{HO} = ((\gamma^2+3)-\gamma^2)\frac{a}{3}\cdot\gamma\cdot\exp(b\cdot\gamma^2). \quad (32)$$

And for HOE:

$$P_{fs}^{HOE} = P_{fs}^{HO} = ((\gamma^2+3)-\gamma^2)\frac{a}{3}\cdot\gamma\cdot\exp(b\cdot\gamma^2)+ + 2a_{ff}\cdot\gamma^3\cdot\exp(b_{ff}\cdot\gamma^4)+a_{fs}\cdot\gamma\cdot\exp(b_{fs}\cdot\gamma^2), \quad (33)$$

$$P_{fn}^{HOE} = ((\gamma^2+3)-\gamma^2)\frac{a}{3}\cdot\gamma\cdot\exp(b\cdot\gamma^2)+ + 2a_{ff}\cdot\gamma^3\cdot\exp(b_{ff}\cdot\gamma^4)+\frac{a_{fn}\cdot b_{fs}}{b_{fn}}\cdot\gamma\cdot\exp(b_{fs}\cdot\gamma^2), \quad (34)$$

$$P_{sf}^{HOE} = P_{SF}^{HO} = ((\gamma^2+3)-\gamma^2)\frac{a}{3}\cdot\gamma\cdot\exp(b\cdot\gamma^2)+ + 2a_{ss}\cdot\gamma^3\cdot\exp(b_{ss}\cdot\gamma^4)+a_{fs}\cdot\gamma\cdot\exp(b_{fs}\cdot\gamma^2), \quad (35)$$

$$P_{sn}^{HOE} = ((\gamma^2+3)-\gamma^2)\frac{a}{3}\cdot\gamma\cdot\exp(b\cdot\gamma^2)+ + 2a_{ss}\cdot\gamma^3\cdot\exp(b_{ss}\cdot\gamma^4)+\frac{a_{sn}\cdot b_{sn}}{b_{fs}}\cdot\gamma\cdot\exp(b_{sn}\cdot\gamma^2), \quad (36)$$

$$P_{nf}^{HOE} = ((\gamma^2+3)-\gamma^2)\frac{a}{3}\cdot\gamma\cdot\exp(b\cdot\gamma^2) + \frac{a_{fn}\cdot b_{fs}}{b_{fn}}\cdot\gamma\cdot\exp(b_{fs}\cdot\gamma^2), \quad (37)$$

$$P_{ns}^{HOE} = ((\gamma^2+3)-\gamma^2)\frac{a}{3}\cdot\gamma\cdot\exp(b\cdot\gamma^2). + \frac{a_{sn}\cdot b_{sn}}{b_{fs}}\cdot\gamma\cdot\exp(b_{sn}\cdot\gamma^2). \quad (38)$$

It should be noted that the HO model does not differentiate between the NF and NS modes (Eq. 32), as it only considers I_{fs}, resulting in identical analytical expressions for the N- modes. On the other hand, the HOE model does provide distinct analytical expressions for the 6 shear configurations, although the FS and SF modes coincide with the standard HO model (Eqs. 33 and 35).

4 Parameter sensitivity analysis

After describing the experimental and mathematical framework, we conducted a sensitivity analysis of the material parameters for every model. We aim to analyze, for each of the deformation modes considered, the impact of each parameter in the selected formulations. This helps to determine which parameters are more influential in each of these modes. As explained in the previous section, we will examine the biaxial conditions as well as the six configurations of the simple triaxial shear tests. We have performed two different types of sensitivity analysis, a local one focused on the parameter values that reproduce the experimental in vitro response presented in [40] and a global sensitivity analysis using Sobol indexes.

4.1 Local parameter sensitivity analysis

We started with an initial set of parameters for each model (Table 1), which were estimated from the biaxial and simple shear tests presented in [17], using the analytical expressions described above. Briefly, the parameters were derived through a least-squares minimization process using the *fmincon* function in Matlab. For further details on this process, the reader is referred to [40] (specifically, the selected values correspond to the *IVT* case in that study).

Then, similar to Gao et al. [24], we imposed a 10% variation on each parameter, both incrementally (C_i^{10+}) and decrementally (C_i^{10-}). Subsequently, we calculated their associated Mean Squared Error (MSE) values and averaged them to determine the

Table 1 Initial mechanical parameter values at the parameter sensitivity analysis for the three selected constitutive models

Costa											
C	b_{ff}	b_{ss}	b_{nn}	b_{fs}	b_{fn}	b_{sn}					
1.884	2.723	1.650	1.320	3.874	2.734	2.964					
HO											
a	b	a_{ff}	b_{ff}	a_{ss}	b_{ss}	a_{fs}	b_{fs}				
2.675	3.302	1.403	5.421	0.143	0.141	0.559	10.931				
HOE											
a	b	a_{ff}	b_{ff}	a_{ss}	b_{ss}	a_{fs}	b_{fs}	a_{fn}	b_{fn}	a_{sn}	b_{sn}
2.048	3.835	1.962	4.295	0.337	0.251	0.878	9.265	0.233	10.245	0.292	9.680

MSE values for each 10% parameter variation ($MSE_i^{10} = \frac{MSE(C_i^{10+}) + MSE(C_i^{10-})}{2}$). Finally, we analyzed the variations with respect to the initial MSE (MSE_0) to quantify the impact of the 10% parameter variation over the initial response ($\Delta MSE = \frac{MSE_0 - MSE_i^{10}}{MSE_0}$). This analysis was quantified for each deformation mode and each material model. We independently analyzed all parameters of each model, so only one was varied at a time. The MSE is defined as

$$MSE = \frac{1}{N_{tests}} \sum_{i=1}^{N_{tests}} \left(\frac{1}{N_{points}} \sum_{i=1}^{N_{points}} \left(\frac{\mathbf{P}_{test} - \mathbf{P}_{an}}{max(\mathbf{P}_{test})} \right)^2 \right), \quad (39)$$

where N_{points} corresponds to the number of points evaluated in each curve, which was fixed to 100 in every term; $\mathbf{P}_{test}$ and $\mathbf{P}_{an}$ represent the already mentioned experimental and analytical values of the PK1 stress tensor for each strain mode, respectively; N_{tests} is the total amount of considered *in vitro* tests for the fitting process. Errors were normalized by the maximum experimental value for the biaxial and shear stresses.

Figure 2a–c shows the results of this parameter sensitivity analysis. For each deformation mode and each constitutive model, the ΔMSE variations of each parameter were computed and normalized from 0 to 1, providing a more intuitive visualization. Therefore, a bigger area means that a specific parameter generated greater MSE increases than the others. To corroborate that this is not a seed-dependent process, the entire study was repeated for different initial parameter values and the conclusions remained consistent.

Starting with the Costa model (Fig. 2a), we observe that several parameters significantly affected the response across all deformation modes. The parameter C was excluded from the analysis since, being outside the exponential term (Eq. 4), it influences all deformation modes equally. In the biaxial modes, only b_{ff}, b_{ss}, and b_{nn} caused changes in MSE, which aligns with Eqs. 16 and 17. Interestingly, b_{ss} presents a great influence on biaxial conditions, although the S direction is not involved in the biaxial extension. This is easily explained by Eqs. 16 and 17, as all b_{ff}, b_{ss}, and b_{nn} are involved in the biaxial PK1 terms. The influence of these three parameters is fairly balanced, as they all generate changes of similar magnitude, fluctuating individually for each loading ratio and between MFD and CFD. Similarly, in the shear modes, the results depend on the parameters presented in Eqs. 22–27. In this case, the entire set of parameters appears, but the shear-related parameters (b_{fs}, b_{fn}, and b_{sn}) dominate the shear response, having much greater weight than the hydrostatic ones.

All this implies that Costa parameters are highly correlated and influence several deformation modes simultaneously. This coupling means that more information is needed to accurately adjust their values, but the model will be more robust in complex deformation modes and may have higher predictive capacity.

In the case of the HO model (Fig. 2b), the individual parameter effects are quite different. All modes are primarily dominated by the isotropic parameters (a and b), showing a much greater impact than the others in almost every loading condition. In the TBx tests, there is minimal influence of a_{ss} and b_{ss} (almost imperceptible in some modes) and moderate influence of a_{ff} and b_{ff} in the MFD direction. Regarding the shear modes, they are almost entirely dominated by the isotropic terms, except for the FS and SF modes where the parameters b_{fs} and a_{fs} do have a significant influence.

Overall, this model does not exhibit high correlation, as, apart from the isotropic terms, the rest of

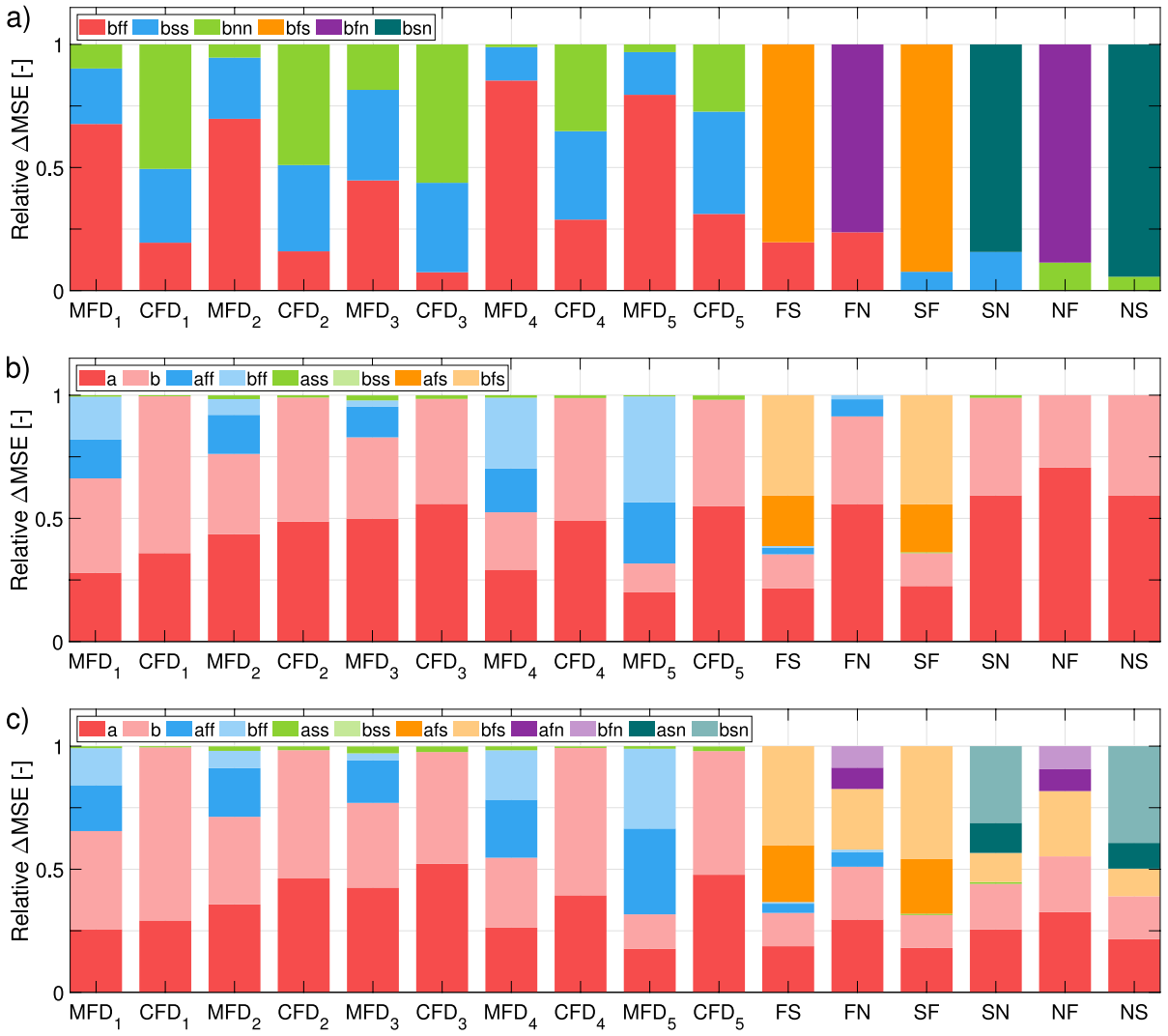

Fig. 2 Sensitivity analysis of the individual parameter impact into the minimization process for the (**a**) Costa, (**b**) HO, and (**c**) HOE formulations

the parameters are highly focused on specific deformation modes (a_{ff}-b_{ff} in MFD and a_{fs}-b_{fs} in FS-SF). However, this model includes parameters that do not influence the deformation modes considered in our study (a_{ss} and b_{ss}), adding unnecessary complexity to the minimization processes. Being the parameters more independent, they are easier to determine from fewer experimental data, especially if the datasets do not include evidently orthotropic data. However, it also implies that the robustness and predictive capacity of the model may be reduced.

Finally, the HOE model (Fig. 2c) shows almost identical results to HO in the biaxial modes, mainly dominated by the isotropic parameters, though less evident in MFD. This makes sense as the difference between the two models lies in the shear terms. In the shear modes, significant differences are observed compared to HO, with HOE showing a more balanced response. In all cases, the parameter b_{fs} has a significant influence, and each complementary set of tests (FS–SF, FN–NF, SN–NS) is individually influenced by the resting shear parameters. Therefore, this model is very versatile in characterizing full sets of shear modes, as each

mode is controlled by different parameters. However, this is achieved by introducing many parameters to the model, which penalizes the efficiency of their estimation process.

To improve the fit of the biaxial modes compared to HO, the inclusion of the remaining term (I_{nn}) could be considered, but this would increase even more the number of constants in HOE by 2 more, which is already high. This could be beneficial for specific studies requiring the characterization of very complex deformation modes if enough fitting data is available.

These differences in the parameter sensitivity of each selected formulation are justified by the approach followed in each model to relate the deformations associated with each strain mode. In Costa's model, all modes are coupled within the same exponential term, achieving an inherent coupling between the microstructural directions. On the other hand, the HO model considers each strain mode in separate terms, which neglects the interaction between the orthotropy directions in non-equibiaxial biaxial tests. This becomes even more evident if, for each model, the partial derivatives of the SEDF are computed for every configuration ($\Psi_{ij} = \frac{\partial \Psi}{\partial I_{ij}}$). For the Costa model, they result in:

$$\Psi_{ff}^{Costa} = \frac{C}{2} b_{ff}(I_{ff} - 1) \cdot e^{Q}, \tag{40}$$

$$\Psi_{ss}^{Costa} = \frac{C}{2} b_{ss}(I_{ss} - 1) \cdot e^{Q}, \tag{41}$$

$$\Psi_{nn}^{Costa} = \frac{C}{2} b_{nn}(I_{nn} - 1) \cdot e^{Q}, \tag{42}$$

$$\Psi_{fs}^{Costa} = \Psi_{sf}^{Costa} = \frac{C}{2} I_{fs} b_{fs} \cdot e^{Q}, \tag{43}$$

$$\Psi_{fn}^{Costa} = \Psi_{nf}^{Costa} = \frac{C}{2} I_{fn} b_{fn} \cdot e^{Q}, \tag{44}$$

$$\Psi_{sn}^{Costa} = \Psi_{ns}^{Costa} = \frac{C}{2} I_{sn} b_{sn} \cdot e^{Q}, \tag{45}$$

where

$$e^{Q} = \exp\left[I_{fn}^2 b_{fn} + I_{fs}^2 b_{fs} + I_{sn}^2 b_{sn} + b_{ff}(I_{ff} - 1)^2 + b_{nn}(I_{nn} - 1)^2 + b_{ss}(I_{ss} - 1)^2\right]. \tag{46}$$

These terms are generic for any deformation state and show which strain pseudo-invariants can potentially influence the deformation state in each direction, regardless of the boundary conditions. This again shows a significant coupling, as all the anisotropic pseudo-invariants appear in each deformation mode.

For the HO model, these expressions are:

$$\Psi_{ff}^{HO} = a_{ff}(I_{ff} - 1) \exp\left(b_{ff}\left(I_{ff} - 1\right)^2\right), \tag{47}$$

$$\Psi_{ss}^{HO} = a_{ss}(I_{ss} - 1) \exp\left(b_{ss}\left(I_{ss} - 1\right)^2\right), \tag{48}$$

$$\Psi_{fs}^{HO} = \Psi_{sf}^{HO} = a_{fs} I_{fs} \exp\left(b_{fs} I_{fs}^2\right), \tag{49}$$

$$\Psi_{fn}^{HO} = \Psi_{sn}^{HO} = \Psi_{nf}^{HO} = \Psi_{ns}^{HO} = \Psi_{nn}^{HO} = 0. \tag{50}$$

Here, it is observed that each direction depends solely on its associated parameter, demonstrating low coupling between directions. Additionally, since only the invariants I_{ff}, I_{ss}, and I_{fs} are considered in its formulation, the directional derivatives are zero for many terms. This means that, although the HO model can perfectly capture the interactions between the orthotropic directions, its ability to represent the complex three-dimensional interaction of myocardial fibers is slightly limited compared to the Costa model. To address this, the extension imposed in the HOE model leads to:

$$\Psi_{ff}^{HOE} = \Psi_{ff}^{HO}, \tag{51}$$

$$\Psi_{ss}^{HOE} = \Psi_{ss}^{HO}, \tag{52}$$

$$\Psi_{nn}^{HOE} = \Psi_{nn}^{HO} = 0, \tag{53}$$

$$\Psi_{fs}^{HOE} = \Psi_{sf}^{HOE} = \Psi_{fs}^{HO} = \Psi_{sf}^{HO}, \tag{54}$$

$$\Psi_{fn}^{HOE} = \frac{a_{fn} b_{fs}}{b_{fn}} I_{fn} \exp\left(b_{fs} I_{fn}^2\right), \tag{55}$$

$$\Psi_{sn}^{HOE} = \frac{a_{sn} b_{sn}}{b_{fs}} I_{sn} \exp\left(b_{sn} I_{sn}^2\right). \tag{56}$$

Here, most directional derivatives are retained, but thanks to the new terms (I_{fn} and I_{sn}), greater versatility is achieved in the shear modes.

Therefore, the Costa model has demonstrated a more balanced response among its parameters in the sensitivity analysis, as all parameters show influence across the deformation modes analyzed. In contrast, certain parameters in the HO-based formulations exhibit limited influence on some of the studied modes (a_{ss} and b_{ss}). Nevertheless, it should be noted that this initial conclusion is highly dependent on the particular experimental dataset. Additionally, considering more coupled models, such as Costa, can pose a problem as it complicates the determination of their parameters due to their higher correlation. This issue can become more pronounced if an extensive experimental dataset is unavailable, such as *in vivo*-based studies [22, 24].

4.2 Global parameter sensitivity analysis

The local sensitivity analysis allowed us to analyze the direct influence of each individual parameter on the fitting of the experimental data for each deformation mode considered. However, this approach is limited to exploring the vicinity of a specific parameter set, which could bias the analysis due to that particular combination of parameters and may not be globally representative. To address this isssue, we also performed a global sensitivity analysis to examine the direct and indirect effects of parameters across a defined range, to contrast its results with the local study at the fitted point. Specifically, we employed Sobol indices [42], which are a well-known global sensitivity metrics. Sobol indexes are based on decomposing the variance of a given function into contributions attributable to each individual input variable and their interactions, providing a comprehensive understanding of the model's sensitivity across an entire input space.

Therefore, for a function $Y = f(X_1, X_2, \ldots, X_n)$, where X_i are referred to the input variables, the total variance $\mathrm{Var}(Y)$ is decomposed into terms associated with the direct individual effects of each input variable (primary Sobol indices, S_i) and the effects associated with their interactions with other input variables (secondary Sobol indices, S_{ij}). Finally, the total-order Sobol index (($S_{Ti} = S_i + S_{ij}$) represents the fraction of the overall response variance, $\mathrm{Var}(Y)$, attributable to any joint parameter variations that include variations of X_i. To compute these indices, an input dataset is generated in which each variable varies within the defined range ($X_i \in [a_i, b_i]$) using methods such as Latin Hypercube Sampling or Sobol Sequences. The variations in the output function's variance are then analyzed for each input variable.

For this input dataset, the first-order indices S_i are defined as the fraction of the total variance attributable to the variable X_i. According to the Saltelli formulation [43], this can be expressed as:

$$S_i = \frac{V_{X_i}\left(E_{\mathbf{X}_{\sim i}}(Y|X_i)\right)}{\mathrm{Var}(Y)}, \tag{57}$$

where X_i is the selected input variable and $\mathbf{X}_{\sim i}$ denotes the matrix of all input variables except X_i. The expectation operator ($E(\cdot)$) refers to the mean of the output function, Y, taken over all possible values of $\mathbf{X}_{\sim i}$ while keeping X_i fixed. The outer variance, $V_{X_i}(\cdot)$, is taken over all possible values of X_i. The interpretation of this expression is that the primary indices, S_i, quantify the fraction of the total variance attributable to the input variableX_i. Similarly, S_{Ti} can be expressed as:

$$S_{Ti} = 1 - \frac{V_{X_{\sim i}}\left(E_{\mathbf{X}_i}(Y|X_{\sim i})\right)}{\mathrm{Var}(Y)}. \tag{58}$$

In [43], it is stated that, in terms of the expected reduction of variance, the term $V_{X_i}\left(E_{\mathbf{X}_{\sim i}}(Y|X_i)\right)$ used in S_i can be interpreted as the expected reduction in variance that would be obtained if X_i could be fixed. Similarly, the term $V_{X_{\sim i}}\left(E_{\mathbf{X}_i}(Y|X_{\sim i})\right)$ used in the second expression can be interpreted as the expected reduction in variance that would be obtained if all factors but X_i could be fixed. Thus, the interpretation of the total-order indices, S_{Ti}, is that they quantify the fraction of the total variance attributable to the variable X_i, including all its interactions with other variables.

In our case, the output functions for analyzing parameter sensitivity, as in the local study, are the analytical solutions developed in the previous sections for the 8 deformation modes considered (the MFD and CFD directions from the biaxial test and the 6 shear modes FS–FN–SF–SN–NS). For these functions, the input variables correspond to the constitutive model's parameters. We analyzed

datasets of 10,000 samples consisting of independent parameter combinations within the defined parametric variation range for each of the three material models. Specifically, three datasets were generated using Latin Hypercube Sampling, each with dimensions $10000 \times k$, where k is the number of parameters for each model (7, 8, and 12 for Costa, HO, and HOE, respectively). To determine the variation range for each parameter, we used their maximum values presented in Appendix A.4. Thus, the studied range spans for all parameters from 0 (as parameters cannot be negative) to twice the maximum value recorded across all experimental cases. Under these conditions, first-order Sobol indices and total Sobol indices were calculated for the 8 deformation modes.

Figure 3 presents the results obtained for the Costa model. The complete numerical values are included in Appendix A.4. The first-order indices (S_i) show a similar trend to that observed in the local sensitivity analysis, although slight differences are evident. The MFD mode is also clearly dominated by the effect of b_{ff}, while in the CFD mode, the effects are primarily distributed between b_{ff} and b_{ss}. This differs slightly from the local study, where the most influential parameters were b_{ss} and b_{nn}. In the shear modes, the shear parameters make the most significant contributions across all modes. In this global analysis, the parameter C_0 was not excluded, and its influence can be clearly seen. While the numerical value of its contribution varies across deformation modes (Appendix A), its influence is comparable for all of them. As previously stated, this is because C_0 multiplies the entire function and appears similarly in all deformation modes.

Therefore, the first-order indices show results with an overall trend similar to the local study, as they also reflect the individual effects of each parameter. Thus, the conclusions from the previous section remain valid. However, certain differences, such as those observed in the CFD mode, indicate the necessity of considering such global approaches

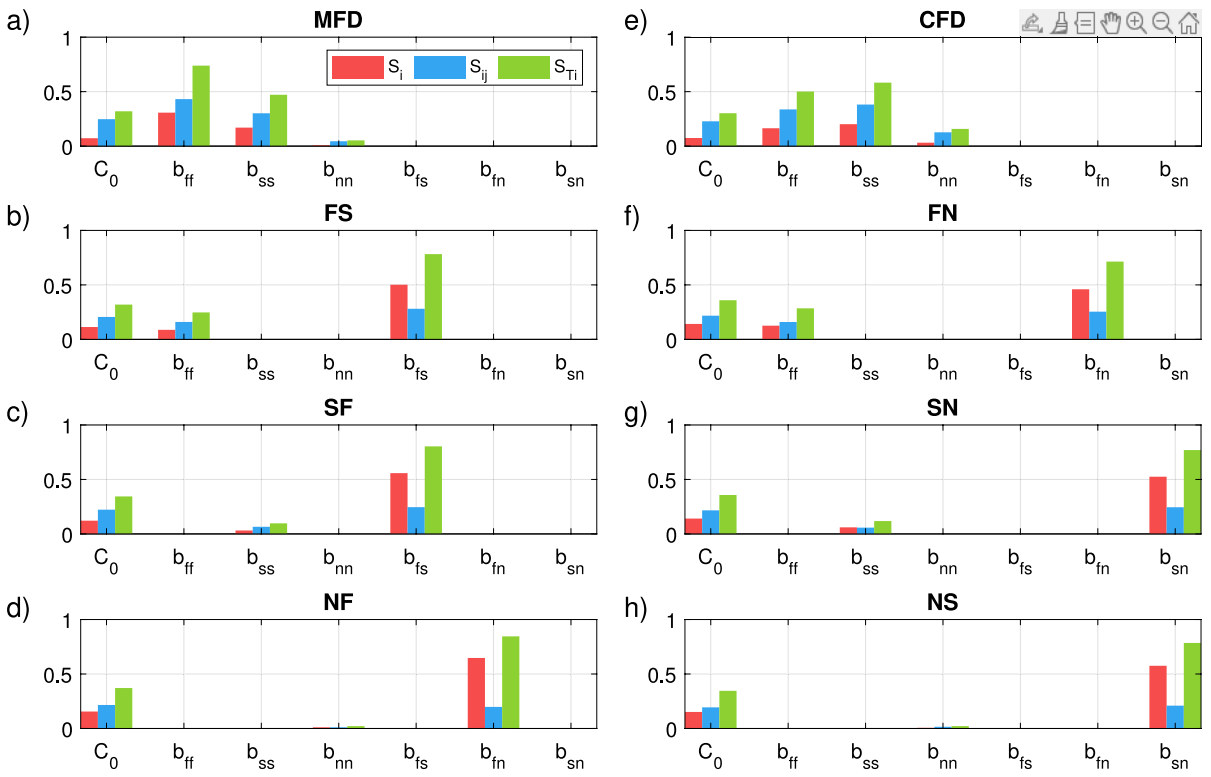

Fig. 3 Calculated Sobol indexes for the Costa material model for the different deformation modes (**a**–**h**). Red bars indicate Sobol first order index values (S_i), blue bars indicate Sobol secondary order index values (S_{ij}), and green bars indicate Total Sobol index values (S_{Ti})

to avoid results biased by individual parameter values, which may not be globally representative.

Regarding parameter interactions (S_{ij}), the values observed are comparable to the first-order indices, suggesting significant interactions between parameters. In the biaxial modes, the secondary effects of the parameters (shown in blue) exceed the direct effects, indicating that the variability of the model is more influenced by interactions among several parameters than by their individual effects. This demonstrates strong correlations between them. In the shear modes, the interactions among dominant parameters are less significant than their individual effects but remain non-negligible. Overall, these results confirm again that, in the Costa model, there is substantial interaction between parameters, confirming the coupling in its formulation.

On the other hand, Fig. 4 shows the results for the HO model. For the first-order indices in the biaxial modes (MFD and CFD), the trend is again similar to the local study, being completely dominated by the isotropic terms (a and b). This trend persists in the shear modes, except for FS and SF, where the parameters specific to these modes (a_{fs} and b_{fs}) dominate the changes in variance, aligning with the previous section. This once again confirms that the HO model is primarily dominated by the isotropic terms, which may make it inefficient for mixed deformation modes or datasets exhibiting significant orthotropy, requiring distinct mechanical responses in each direction.

Regarding the effects of parameter interactions (S_{ij}), these are much smaller than the direct effects (S_i) for the HO model in nearly all deformation modes. This confirms a lower correlation and a weaker coupling of the HO model compared to Costa's. Again, while this may make it easier to obtain objective parameters from limited data, it could also reduce its ability to predict mixed deformation modes, as previously mentioned.

Finally, Fig. 5 shows the results for the HOE model. The biaxial modes exhibit an identical trend to the HO model since, as mentioned earlier, the

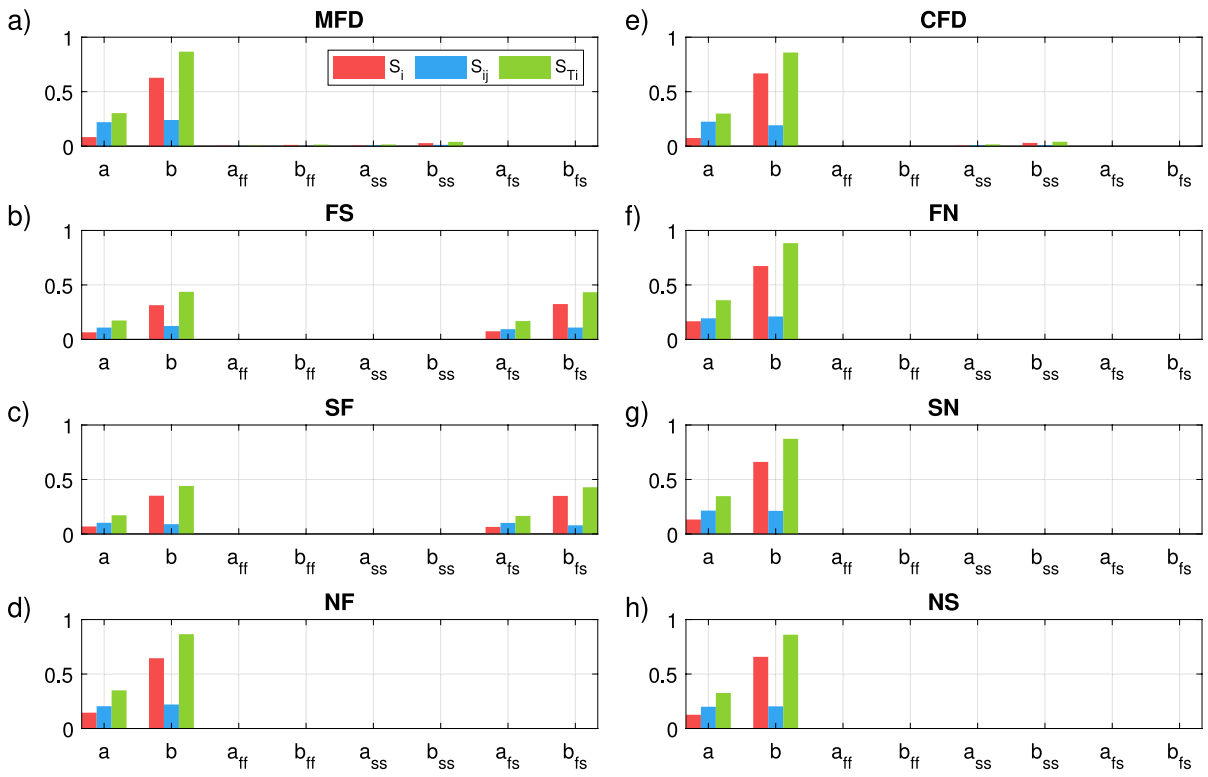

Fig. 4 Calculated Sobol indexes for the HO material model for the different deformation modes (**a**–**h**). Red bars indicate Sobol first order index values (S_i), blue bars indicate Sobol secondary order index values (S_{ij}), and green bars indicate Total Sobol index values (S_{Ti}

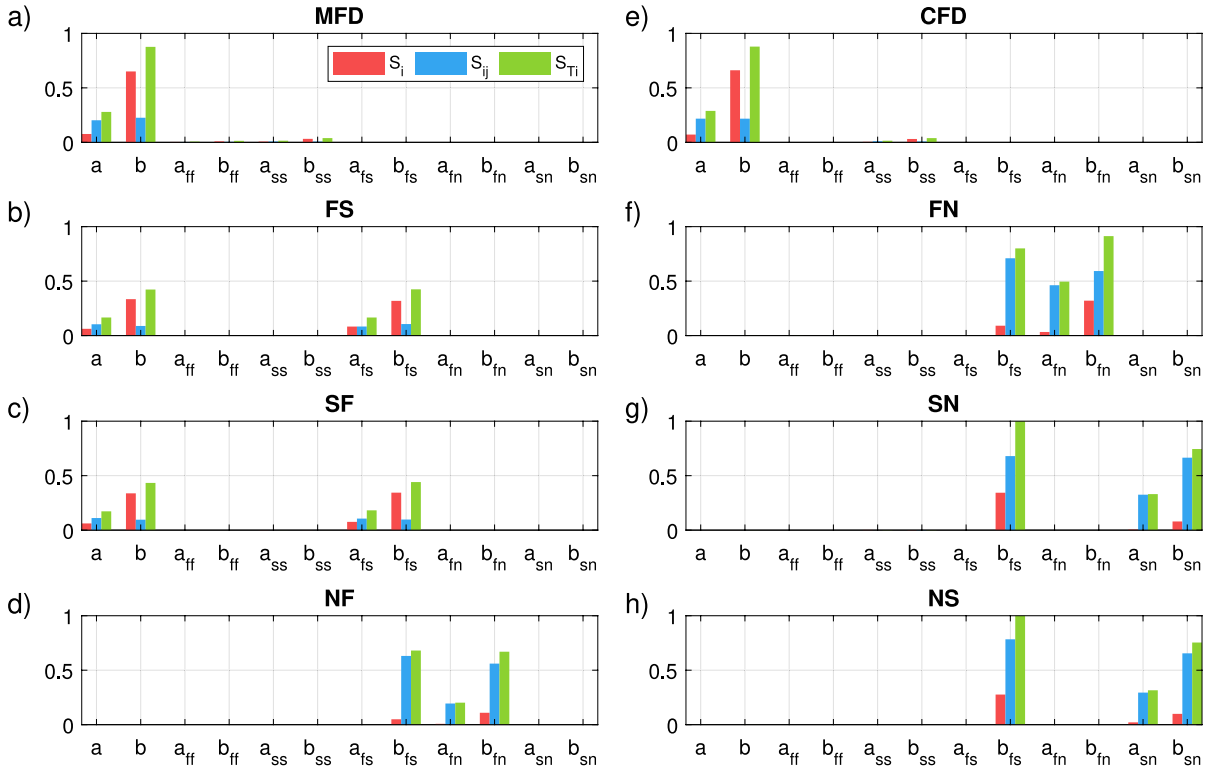

Fig. 5 Calculated Sobol indexes for the HOE material model for the different deformation modes (**a**–**h**). Red bars indicate Sobol first order index values (S_i), blue bars indicate Sobol secondary order index values (S_{ij}), and green bars indicate Total Sobol index values (S_{Ti})

formulation changes in the HOE model lie in the inclusion of additional shear terms. In the case of the shear modes, significant changes are observed due to the inclusion of these new shear terms. Similar to the local study, both the direct effects and the interaction effects are dominated in each case by the shear parameters specific to each mode. It is worth noting that the parameter b_{fs} has a significant influence across all shear modes. The results for the secondary indices (S_{ij}) indicate that, in the HOE model, there is also a significant interaction between parameters in the shear modes, with values far exceeding the first-order indices in almost all modes, similar to the Costa model. Thus, the correlation of the new parameters added in this formulation of the HO model is greater than in the original version. The trends shown in the graphs in Fig. 5 are consistent with those observed in the local study.

The results of the global study using Sobol indices confirm the conclusions of the local study while adding new relevant information for comparing different material models. The Costa model has once again demonstrated a more homogeneous distribution of variations in variance compared to the HO-type formulations, which remain predominantly dominated by the isotropic parameters. Furthermore, the analysis of parameter secondary effects has shown that the Costa and HOE models exhibit greater interactions between parameters than the HO model, suggesting stronger coupling in their formulation. Therefore, although all three models adequately fit the biaxial and shear datasets considered, the Costa model appears to provide slightly superior performance and, if the input data is sufficiently robust, may offer greater predictive capability for mixed deformation modes.

5 Constitutive law performance against different experimental inputs

The sensitivity analysis evidenced that the impact of each parameter across the three models differs

significantly. The Costa model exhibits strong parameter coupling, resulting in a balanced distribution across all deformation modes. In contrast, the HO and HOE models show a response predominantly influenced by the isotropic component of their formulations, with some parameters having localized importance in specific deformation modes. Between the two, the standard HO model shows limited versatility in capturing distinguished orthotropic behaviors, which is compensated in the HOE model, though at the cost of introducing 4 more parameters. However, these parameters tend to be more independent of each other than in Costa's formulation, which may complicate the determination of unique solutions in this latter case, if an adequately large experimental dataset is not available.

This confirms that the performance of these models in replicating experimental data, and consequently the selection for a numerical-experimental study, is influenced by the type of data considered. Therefore, as stated above, we considered 5 different types of input data for the three selected models, based on the most common *in vitro* methodologies for myocardium: (i) Equibiaxial tests [4–6]; (ii) True biaxial tests [7–13]; (iii) Simple triaxial shear tests [14, 15]; (iv) Combined Data 1 (CMB1): combining equibiaxial and shear results; (v) Combined Data 2 (CMB2): combining true biaxial and shear results [16, 17]. We aim to analyze how the three selected models perform with purely biaxial data (i and ii), purely shear (iii), or a combination of both (iv and v). In all cases, an inverse estimation of the mechanical parameters for each model was performed (see Sect. 4). The data not included in the fitting process were used to validate the predictive and extrapolative power of the obtained parameters. For biaxial-only based cases (i and ii), STS tests could not be predicted, as the mechanical shear parameters could not be characterized (Eqs. 16–17 and Eqs. 19–20). Figure 6 provides a summary of the fitted and predicted data for each case.

Within these 5 groups, we selected data from individual experimental tests. Out of the 7 animals described in [17] for which medial data were acquired, we selected a total of 5 for our study, corresponding to those with a complete set of simple shear tests. For each of these 5 animals, in addition to the full shear dataset, we selected two sets of biaxial results, resulting in 10 data combinations across all groups analyzed. To evaluate each model's response, we derived their mechanical parameter values for every individual dataset. These 10 datasets are sufficiently comprehensive to encompass diverse mechanical responses in terms of stiffness and orthotropy within the typical deviation range of the tissue. The data used have already been shown to be comparable to other experimental studies [17], such as those by Dokos [14] or Sommer [16]. Therefore, contrasting the results with such studies was not considered necessary, as they are already covered by the 10 datasets analyzed.

Additionally, three different metrics were chosen to quantify the fitting accuracy. First, we considered the Mean Squared Error (MSE) between the selected normalized *in vitro* experiments and their analytical expressions for each strain mode as stated in Eq. 39. Second, the goodness of fitting was also assessed by the coefficient of determination, (R^2), which is defined as

$$R^2 = 1 - \frac{\sum_{i=1}^{N}(Y_i - \hat{Y})^2}{\sum_{i=1}^{N}(Y_i - \bar{Y})^2}, \tag{59}$$

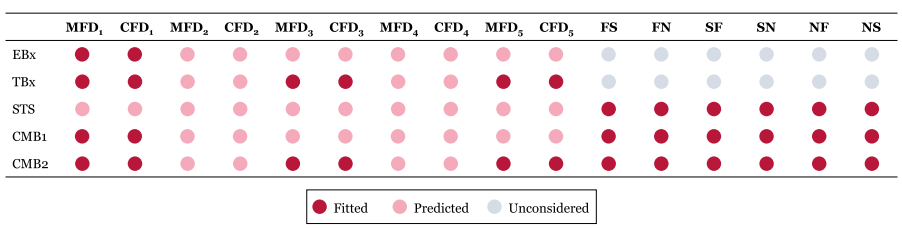

Fig. 6 Considered experimental inputs in each case: Equibiaxial dataset (EBx), True Biaxial dataset (TBx), Simple Triaxial Shear dataset (STS), Combined dataset 1 (CMB1): EBx + STS, and Combined dataset 2 (CMB2): TBx + STS. MFD_i and CFD_i correspond to each of the biaxial loading ratios explained above

where Y correspond to the reference experimental values, $\hat{Y}$ to the simulated values, $\bar{Y}$ to the mean experimental value and N to the number of considered points (n=100).

Although R^2 and MSE are suitable for assessing the goodness of fit, they do not consider the number of parameters in each model. Besides achieving an accurate fit to the experimental response, is essential to minimize the number of considered parameters to avoid overfitting. Therefore, we also considered the Akaike Information Criterion (AIC) [44] to account for the number of parameters used in each model. This criterion has already been used for statistical analysis in cardiac tissue characterization and simulation studies [34, 35, 45–47]. The AIC penalizes models with more parameters, favoring those that provide a good fit with the fewest parameters, and is given by:

$$\mathrm{AIC} = 2k - 2\log(MSE), \tag{60}$$

where MSE is the obtained mean squared error and k is the number of parameters each model uses (7, 8, and 12 for Costa, HO, and HOE, respectively).

Similar to the approach by Schmid et al. [34, 35], we also analyzed the variability of both the individual values of the mechanical parameters and the three considered metrics across the individual samples in each case (n=10). To do this, we calculated their mean value ($Mean$) and standard deviation (SD) across all specimens and obtained the coefficient of variation ($\bar{V}$) as

$$\bar{V} = \frac{SD}{Mean}. \tag{61}$$

5.1 Biaxial-based analysis

As described in Fig. 6, in the two cases based exclusively on biaxial data (both equibiaxial and true biaxial), certain ratios were considered in the fitting process, while the remaining ones were used to validate the predictive capacity. Simple triaxial shear data were not included in these studies.

Figure 7 shows the average values of all metrics analyzed across all specimens (n=10) for the equibiaxial and true biaxial cases. The numerical values are summarized in Table 2. All the results throughout this study have been included in the Appendix. The results are similar across the three constitutive models, with some slight differences. In both experimental cases, the fitting goodness achieved by all models is comparable (MSE and R^2, see Fig. 7b, c–f, g). All of them provide a highly accurate fit to the data, although with a better fit in the equibiaxial-based scenario (R^2 >0.995 for equibiaxial and R^2 >0.96 for true biaxial) since only one biaxial mode was included in the parameter obtention process in that case. For the predicted data, while a sufficiently accurate response was obtained in the equibiaxial-based case (R^2 >0.92), the predictive capacity improves significantly in the true-biaxial-based approach when non-equibiaxial data are included in the parameter determination process. The MSE values are also consistent with the trends observed in R^2. Therefore, no appreciable variations are observed between the three models in terms of fitting quality (MSE and R^2).

However, although the fitting goodness achieved is similar, it is important to note that the Costa model

Table 2 Costa, HO & HOE performance summary for biaxial-based data (equibiaxial and true biaxial). $max(\bar{V})$ is the maximum variability recorded in the parameter values for the 10 individual datasets. f and p sub-indexes correspond to fitting and prediction results, respectively

	$max(\bar{V})$	MSE_f	Mse_p	R^2_f	R^2_p	AIC_f	AIC_p
EBx							
Costa	0.37	0.07 ± 0.12	0.44 ± 0.27	0.995 ± 0.01	0.92 ± 0.09	14.87 ± 2.64	9.93 ± 1.16
HO	1.03	0.01 ± 0.01	0.46 ± 0.41	0.999 ± 0.01	0.92 ± 0.11	21.11 ± 1.58	14.15 ± 1.56
HOE	1.06	0.01 ± 0.01	0.46 ± 0.41	0.999 ± 0.01	0.92 ± 0.11	21.11 ± 1.58	14.15 ± 1.56
TBx							
Costa	0.42	0.31 ± 0.25	0.25 ± 0.26	0.96 ± 0.05	0.97 ± 0.02	10.82 ± 1.41	11.35 ± 1.49
HO	0.63	0.26 ± 0.20	0.20 ± 0.18	0.96 ± 0.06	0.98 ± 0.02	15.23 ± 1.52	15.81 ± 1.57
HOE	0.63	0.26 ± 0.20	0.20 ± 0.18	0.96 ± 0.06	0.98 ± 0.02	15.23 ± 1.52	15.81 ± 1.57

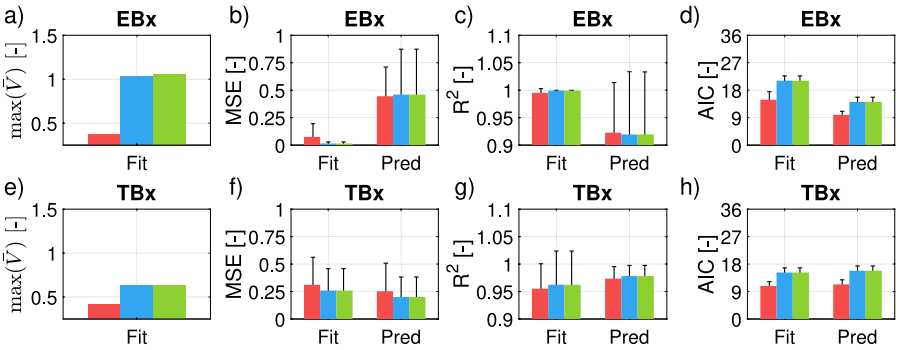

Fig. 7 Summary of the global contrasted metrics for biaxial-based cases (EBx and TBx). max($\bar{V}$) stands for the maximum variability coefficient in the mechanical parameters of each model. In all plots, the red color corresponds to the Costa model, blue to the HO one, and green to the HOE one

uses only 4 parameters in the biaxial expressions, while the HO and HOE models use up to 6 parameters (see Sect. 3.1). Thus, the Costa model achieves an equivalent fitting goodness with two fewer parameters. This is quantified by the AIC (see Fig. 7d–h), as the Costa model shows lower AIC value (see the last two columns of Table 2). Finally, when analyzing the variability in the numerical values of each model parameters, we observe that the Costa model is slightly more stable than the other two, as the maximum recorded variations ($max(\bar{V})$) are smaller in both equibiaxial-based and true-biaxial-based cases (see the first column of Table 2). This suggests that the Costa model is more stable in the presence of small variations in the input data [18].

Therefore, the results demonstrate that when purely biaxial experimental data is considered, all three models offer acceptable fits. Despite the higher coupling between the Costa model parameters, it also delivers a comparable response to HO and HOE models, even in cases where a limited amount of experimental data is available (such as the equibiaxial-based case). On the other hand, the HO-type models have also shown their ability to adequately fit and predict both equibiaxial and non-equibiaxial data, which was questioned in [39] when handling non-equibiaxial datasets. Overall, this suggests that any of the three models is suitable for this type of input data. However, the Costa model is slightly superior when considering the model stability ($max(\bar{V})$) and the number of parameters (AIC). Nevertheless, we would not suggest using only biaxial data, as it does not allow for a complete three-dimensional characterization, nor a complete fitting of all the parameters in each model. Therefore, the inclusion of three-dimensional data, such as those from simple shear tests, is essential.

5.2 Shear-based analysis

We continued our analysis by evaluating the response of all models to purely shear data (STS). This time, all shear data were included in the parameter obtention process, and we attempted to predict the true biaxial response from these data (Fig. 6).

Figure 8a–d shows the average values for all the metrics analyzed, while Table 3 contains the numerical values. Once again, the results are similar for all three models. All of them provide a good fit to the shear data, with R^2 values of 0.96 for Costa and HOE, and 0.94 for HO. However, when examining the individual fitting curves shown in Fig. 10, it becomes evident that the HO presents less accuracy in some of the shear modes compared to Costa or HOE, as it lacks parameters influencing these modes (Fig. 2). For the predicted data, none of the models can correctly predict the biaxial response based solely on shear data (Fig. 9), with the Costa model showing the greatest error. As a result, the recorded MSE values are significantly higher, and in fact, in Fig. 8b, the plotting scale had to be adjusted to display the values. Therefore, these results suggest that to accurately predict the tissue's response in both deformation modes they should be combined. Given that both shear and biaxial stresses occur during ventricular expansion and contraction [16, 37, 48], we believe that it is crucial to consider both deformations simultaneously. This combined approach has already been experimentally applied in previous studies [16, 17].

In shear modes, the Costa model uses all of its 7 mechanical parameters, the HO model 8, and the HOE model 12 (see Sect. 3.1). Thus, the AIC values achieved by the HO and Costa models are similar, while the HOE model is higher due to having significantly more fitting parameters (see the last two

Table 3 Costa, HO & HOE performance summary for simple-shear-based data (STS). $max(\bar{V})$ is the maximum variability recorded in the parameter values for the 10 individual datasets.

	$max(\bar{V})$	MSE_f	MSE_p* (x10^3)	R^2_f	R^2_p	AIC_f	AIC_p
Costa	0.92	0.24 ± 0.28	6.04 ± 7.82	0.96 ± 0.03	0.01 ± 0.007	18.34 ± 2.70	1.35 ± 6.96
HO	0.85	0.29 ± 0.19	1.45 ± 0.59	0.94 ± 0.04	0.009 ± 0.003	19.13 ± 1.97	1.58 ± 0.75
HOE	1.15	0.23 ± 0.19	1.07 ± 0.27	0.96 ± 0.02	0.008 ± 0.005	27.70 ± 2.02	10.11 ± 0.52

f and *p* sub-indexes correspond to fitting and prediction results, respectively

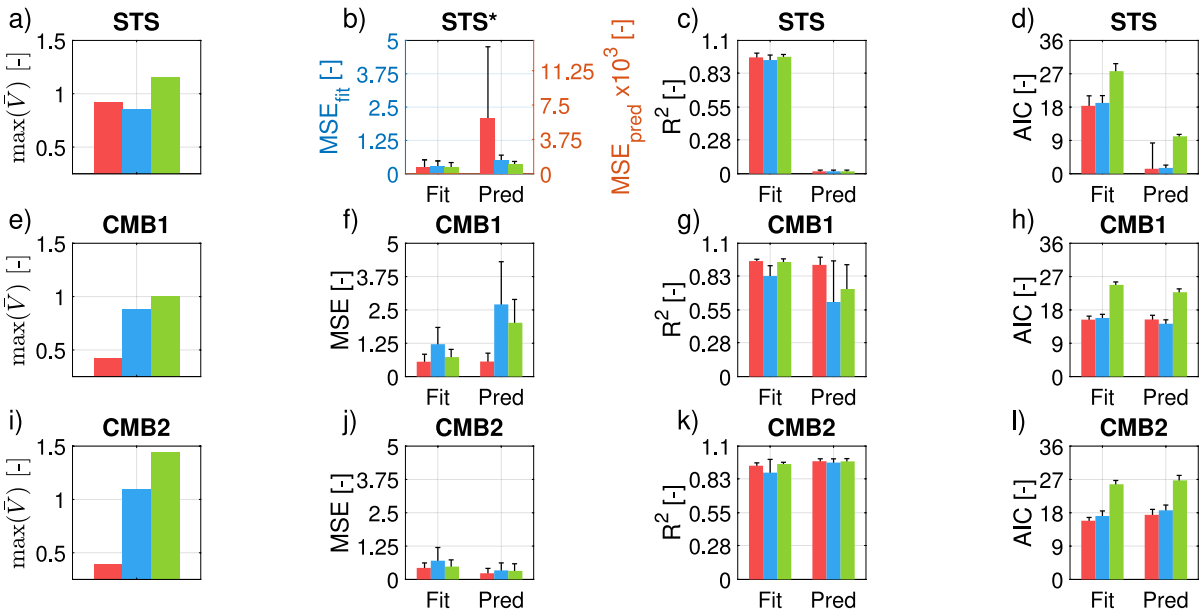

Fig. 8 Summary of the global contrasted metrics for shear-based (STS) and combined (CMB1 and CMB2) cases. max($\bar{V}$) stands for the maximum variability coefficient in the mechanical parameters of each model. In all plots, the red color corresponds to the Costa model, blue to the HO one, and green to the HOE one

columns of Table 3). It is important to note that the AIC is formulated for low MSE values (around 0-1), so while the prediction AIC values may appear very low in all cases, these particular results are not valid.

Regarding the variability of the mechanical parameters, all models show similar stability, with the HO model being slightly more stable than the others in this case (see the first column of Table 3).

Therefore, if the input data are exclusively shear-based, all three models show similar fitting capabilities and stability, without any of them being significantly better than the others. Compared to the biaxial-based cases, the HO and HOE models have improved their performance relative to the Costa when fitting the simple shear datasets, showing greater stability in their parameter estimation and better predictive ability for biaxial responses (although none of the three are sufficiently accurate in this regard). This makes sense as these models were developed based on the experimental data of Dokos et al. [14], so their performance is better suited to these conditions [37]. However, as mentioned earlier, we believe that it is necessary to consider both types of data simultaneously to obtain robust mechanical parameters.

It is also worth noting that, when considering the number of parameters (AIC), the HOE model shows worse fitting performance than the other two. Therefore, the HOE approach should only be considered in cases where the standard HO model is not sufficiently

accurate for the given data. Nonetheless, as Li et al. [19] indicated, if additional deformation modes such as pure shear are considered, the standard HO model may not be robust enough to capture the experimental response. In such cases, the HOE model may be an interesting alternative.

5.3 Combined analysis

Finally, we analyzed cases where biaxial and shear data are combined. We considered two combinations where all the shear data are included in the parameter obtention process along with either the equibiaxial ratio data (CMB1) or the complete true biaxial data (CMB2). In both cases, only part of the biaxial test ratios are predicted (see Fig. 6).

Once again, Fig. 8e–l shows the average results for both cases, and Table 4 contains their numerical values. For the CMB1 results, the Costa model shows the best performance in both fitting and prediction, followed by HOE and HO (columns 2–5 of Table 4). Notably, the Costa model demonstrates to have notably better prediction capacity compared to the other two (8f, g), reinforcing its superior ability to predict non-equibiaxial data [39]. Importantly, by including the equibiaxial data, the errors in predicting biaxial data are drastically reduced compared to the shear-based only case (8b), with errors now being of the same order for both fitting and prediction. However, the fitting error increases slightly compared to the shear-based case, although the values remain reasonable.

In the CMB2 case, where non-equibiaxial data curves are included in the parameter fitting process, the quality of the fit and the errors improve compared to CMB1 (8j, k). In this scenario, the HOE and Costa models perform quite similarly, while the HO model is slightly less accurate, particularly in the fitted data (e.g., looking at the R^2 values in Table 4). Again, although the fitting goodness is comparable for the three models, when considering the number of parameters with the AIC index, the Costa and HO models have similar values, while the HOE one has a higher AIC error both in CMB1 and CMB2.

In terms of parameter stability, the combined cases once again reveal pronounced differences between the Costa model and the HO-type ones. This confirms that in the presence of biaxial data, HO-type models show greater instability in their parameter values compared to Costa's.

Therefore, the results from the combined groups have shown that all three models are capable of simultaneously reproducing biaxial and shear data with acceptable accuracy. In all cases, average R^2 values around 0.9 (at minimum) were obtained, except for the HO model when only equibiaxial data were included (CMB1). We also demonstrated that, including biaxial data, significantly improves the predictive capacity compared to the shear-based only case, even in CMB1. The HOE model shows notable improvements over the HO model in both fitting and prediction capacity, though at the cost of 4 additional parameters. On the other hand, the Costa model demonstrates the best performance, achieving the highest accuracy with respect to the experimental data, using the fewest number of parameters, and exhibiting the greatest stability in the mechanical parameters values.

5.4 On the specific material model selection

We also evaluated the response of the three compared models to several types of *in vitro* experimental data, aiming to identify which one offers a better response for each type of data considered. We compared cases based solely on biaxial data, solely on shear data, and two combinations of both. We observed that using only biaxial data is insufficient, as it does not allow for the characterization of all the mechanical parameters that appear in the constitutive models, while using only shear data does not enable accurate prediction of biaxial conditions. Therefore, we concluded that combined datasets are necessary to ensure a robust parameter estimation for the type of deformations happening in the cardiac cycle.

The Costa model demonstrated a slightly superior response across all analyzed modes, offering comparable fits (albeit slightly lower) for purely biaxial and purely shear data compared to HO-type models. Furthermore, that model provides better fits in combined datasets, especially in terms of predictive capacity, at least for the deformation modes considered in our study. Additionally, this model showed superior stability in parameter estimation compared to the HO-type models, although the three models considered were sufficiently stable. Finally, when considering the number of parameters (AIC), it becomes evident that the Costa model offers a better response, as

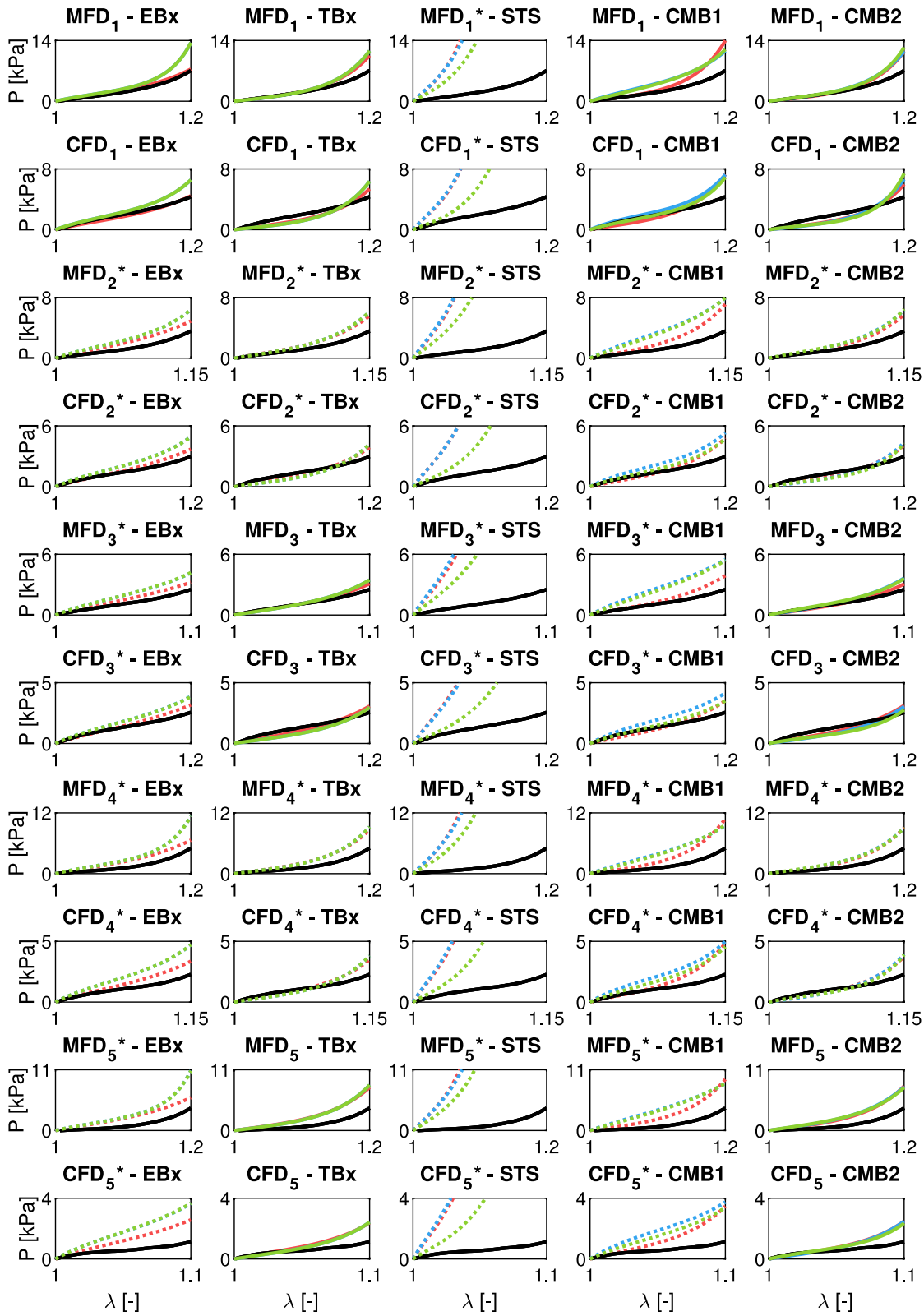
MFD1 - EBx
MFD1 - TBx
MFD1* - STS
MFD1 - CMB1
MFD1 - CMB2
CFD1 - EBx
CFD1 - TBx
CFD1* - STS
CFD1 - CMB1
CFD1 - CMB2
MFD2* - EBx
MFD2* - TBx
MFD2* - STS
MFD2* - CMB1
MFD2* - CMB2
CFD2* - EBx
CFD2* - TBx
CFD2* - STS
CFD2* - CMB1
CFD2* - CMB2
MFD3* - EBx
MFD3 - TBx
MFD3* - STS
MFD3* - CMB1
MFD3 - CMB2
CFD3* - EBx
CFD3 - TBx
CFD3* - STS
CFD3* - CMB1
CFD3 - CMB2
MFD4* - EBx
MFD4* - TBx
MFD4* - STS
MFD4* - CMB1
MFD4* - CMB2
CFD4* - EBx
CFD4* - TBx
CFD4* - STS
CFD4* - CMB1
CFD4* - CMB2
MFD5* - EBx
MFD5 - TBx
MFD5* - STS
MFD5* - CMB1
MFD5 - CMB2
CFD5* - EBx
CFD5 - TBx
CFD5* - STS
CFD5* - CMB1
CFD5 - CMB2
P [kPa]
λ [-]

◂**Fig. 9** TBx experimental data fit for the 5 considered cases for a representative specimen. In each case, the fitted data that were included in the parameter obtention process are plotted in solid lines, while the predicted data are plotted in dotted lines and have been marked (*) in the plot title. MFD_i and CFD_i correspond to each of the biaxial loading ratios explained above. In all plots, red lines correspond to Costa, blue ones to HO, and green ones to HOE

it requires fewer parameters to achieve similar or even better fits. However, all three models have proven accuracy, robustness, and stability enough to fit the various datasets satisfactorily, making all of them valid options for modelling *in vitro* data inputs. Therefore, the Costa model offers a better response, especially when biaxial data are included. However, it is important to note that these conclusions highly depend on the input data type. The model selection may differ if other data types, such as pure shear data [18, 19], or *in vivo* data [22, 24] are included.

Another point to consider is that Costa's mechanical parameters are more strongly coupled than those of the HO-type models (see Sect. 4). While this greater coupling may lead to better performance, it can also complicate the determination of a unique solution in the inverse fitting problem [24, 40]. Therefore, in cases where experimental data are limited or where mechanical properties inference is less direct, as in *in vivo*-based studies, HO-type models with more independent parameters may be more useful.

Between the HO and HOE models, we observed that the inclusion of extra terms in the HOE model significantly improves its performance in several cases. However, the final total number of parameters is considerable, so care must be taken to avoid overfitting. The HOE model shows advantages in some of the shear modes, as its response in biaxial modes is equivalent to HO one. Therefore, we would mainly recommend its use in studies involving clearly orthotropic responses, where the shear modes differ significantly from one to another. In cases where the behavior is closer to a transversely isotropic behavior, the inclusion of the extra terms in the HOE model does not offer obvious advantages.

It is also worth noting the growing number of studies focusing on a different approach based on data-driven models rather than on the optimization or selection of "expert models" tailored to each study. In cardiovascular modeling, multiple studies have already been conducted in this direction [49–51], which show promising results that can be a major step forward in modeling cardiac physiology in the future. However, there still are numerous studies [52–55] based on these "expert models" that provide significant insights to cardiac physiology as well. Moreover, data-driven approaches require much more experimental data than model-based ones. These experimental results are not available on many occasions, especially when they are difficult and expensive to get as happens in biological tissue modeling. Hence, we believe that, at present, both approaches are necessary and deliver valuable findings to the scientific community. Nonetheless, data-driven models should not be overlooked.

Table 4 Costa, HO & HOE performance summary for combined data (CMB1 and CMB2). $max(\bar{V})$ is the maximum variability recorded in the parameter values for the 10 individual datasets.

	$max(\bar{V})$	MSE_f	MSE_p	R^2_f	R^2_p	AIC_f	AIC_p
CMB1: STS + EBx							
Costa	0.42	0.56 ± 0.28	0.57 ± 0.31	0.95 ± 0.01	0.92 ± 0.06	15.37 ± 0.95	15.42 ± 1.13
HO	0.89	1.21 ± 0.63	2.71 ± 1.60	0.83 ± 0.09	0.62 ± 0.34	15.83 ± 0.98	14.27 ± 1.06
HOE	1.00	0.73 ± 0.29	2.02 ± 0.88	0.95 ± 0.03	0.72 ± 0.20	24.77 ± 0.79	22.78 ± 0.91
CMB2: STS + TBx							
Costa	0.40	0.43 ± 0.19	0.23 ± 0.18	0.94 ± 0.02	0.98 ± 0.02	15.85 ± 0.89	17.44 ± 1.47
HO	1.09	0.70 ± 0.49	0.34 ± 0.28	0.88 ± 0.11	0.96 ± 0.03	17.13 ± 1.36	18.66 ± 1.42
HOE	1.44	0.48 ± 0.25	0.32 ± 0.27	0.95 ± 0.01	0.97 ± 0.02	25.70 ± 1.02	26.75 ± 1.34

f and *p* sub-indexes correspond to fitting and prediction results, respectively

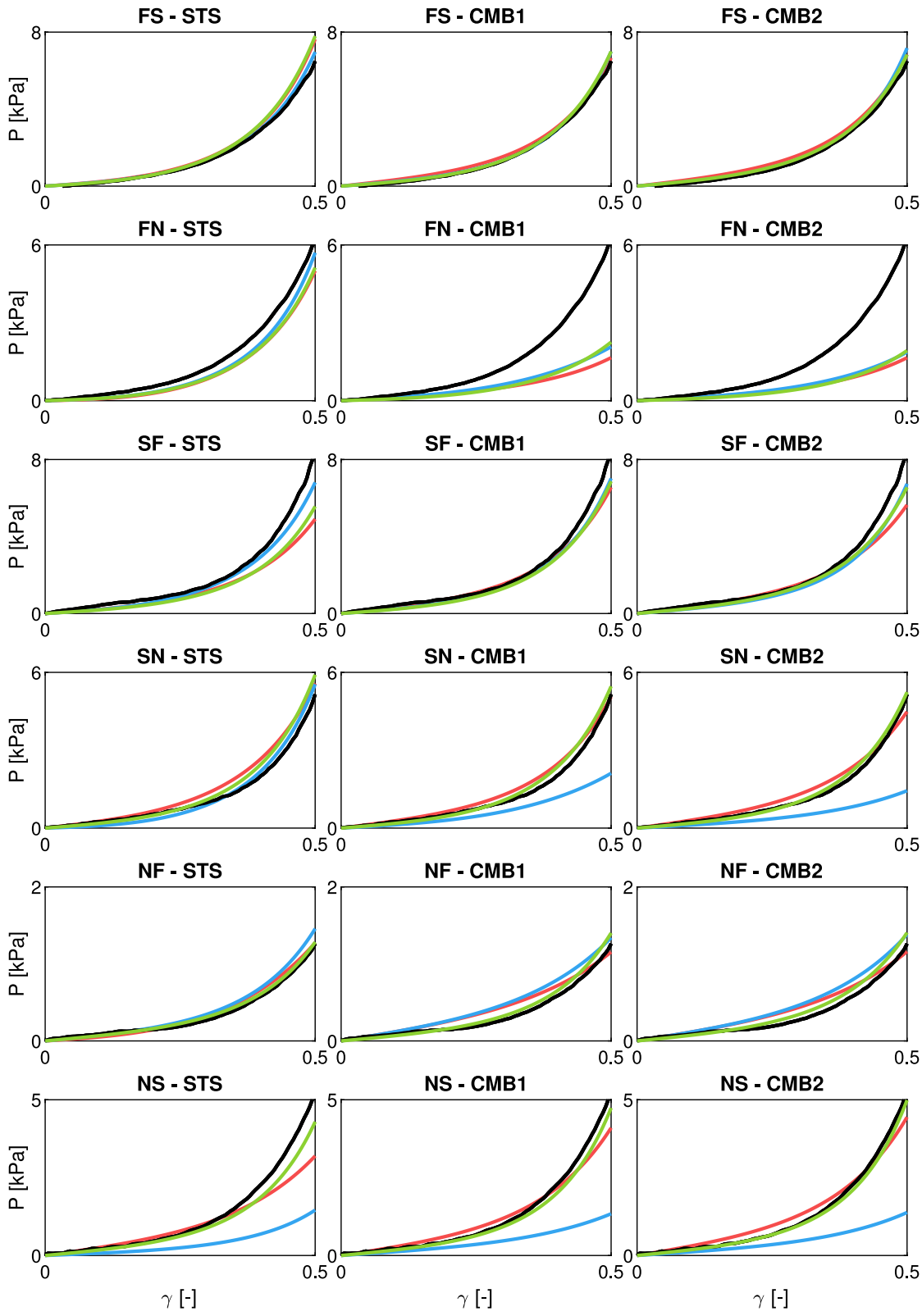
FS - STS
FS - CMB1
FS - CMB2
FN - STS
FN - CMB1
FN - CMB2
SF - STS
SF - CMB1
SF - CMB2
SN - STS
SN - CMB1
SN - CMB2
NF - STS
NF - CMB1
NF - CMB2
NS - STS
NS - CMB1
NS - CMB2
P [kPa]
γ [-]

◂**Fig. 10** Shear experimental data fit for the 5 considered cases for a representative specimen. In each case, the fitted data that were included in the parameter obtention process are plotted in solid lines. In all plots, red lines correspond to Costa, blue ones to HO, and green ones to HOE

6 Conclusions

We have conducted an extensive study on the response of three of the most widely used orthotropic constitutive models for myocardial tissue (Costa, HO, and HOE) to evaluate their fitting and predictive capabilities across five dataset types, which consisted of different combinations of biaxial and shear experimental data from porcine biopsied LV myocardial tissue. Our study shows that, although all models are valid, Costa's formulation presents slight advantages for all the cases considered compared to the HO-type models, as it offers slightly more accurate fits of the experimental data while using fewer parameters in its formulation.

Acknowledgements This work is supported by the European Union's Horizon 2020 research and innovation program under grant agreement 874827 (research project BRAV3, C1-BHC-07-2019, H2020); the Next Generations fund of the Spanish Ministry of Science and Innovation through the Cardioprint Project, PLEC2021-008127 and the Spanish Ministry of Economy and Competitiveness through research project PID2022-140219OB-I00. The authors gratefully acknowledge research support from the ICTS "NANBIOSIS", specifically by the Tissue & Scaffold Characterization Unit (U13) of the CIBER in Bioengineering, Biomaterials & Nanomedicine (CIBER-BBN at the University of Zaragoza). The Instituto de Salud Carlos III finances CIBER Actions with assistance from the European Regional Development Fund. Authors would also like to gratefully thank our laboratory technicians C. Marzo and A. Aparici. Authors also thank J. Ayensa-Jiménez for his help with the parameter sensitivity analysis, as well as the Experimental Surgery Service of the Aragon Health Sciences Institute.

Funding Open Access funding provided thanks to the CRUE-CSIC agreement with Springer Nature.

A Appendix

We include the complete results for all the cases compared throughout the article for the three material models studied. In each case, the individual values of the mechanical parameters for each material are presented, as well as the three metrics analyzed (MSE, R^2, and AIC) for both the fitted and predicted data. For all these variables, and for the five cases, the average values for all specimens (n=10), their standard deviation, and their variability coefficient are provided.

A.1 Costa model complete results

See Tables 5, 6, 7, 8, 9.

Table 5 **Costa** Individual fits (**EBx**)

	C0	bff	bss	bnn	bfs	bfn	bsn	MSE_f	MSE_p	R^2_f	R^2_p	AIC_f	AIC_p
D1	3.38	1.44	1.31	0.66	–	–	–	0.12	0.82	0.98	0.68	12.30	8.40
D2	1.58	2.42	2.17	1.30	–	–	–	0.02	0.27	1.00	0.97	15.74	10.65
D3	1.68	2.42	2.04	1.19	–	–	–	0.01	0.26	1.00	0.98	16.72	10.67
D4	2.19	2.05	1.86	1.69	–	–	–	0.05	0.27	1.00	0.98	14.17	10.62
D5	1.45	3.62	1.41	1.27	–	–	–	0.04	0.40	1.00	0.95	14.43	9.83
D6	1.78	2.85	2.31	0.82	–	–	–	0.02	0.40	1.00	0.96	16.02	9.83
D7	1.61	4.28	0.72	0.65	–	–	–	0.40	0.81	0.98	0.86	9.82	8.43
D8	1.13	3.82	1.58	0.94	–	–	–	0.01	0.23	1.00	0.93	18.27	10.97
D9	1.89	2.58	1.61	1.20	–	–	–	0.01	0.17	1.00	0.98	18.03	11.50
D10	1.08	3.08	2.78	1.70	–	–	–	0.08	0.82	1.00	0.94	13.16	8.39
Mean	1.78	2.86	1.78	1.14	–	–	–	0.07	0.44	1.00	0.92	14.87	9.93
SD	0.65	0.86	0.59	0.38	–	–	–	0.12	0.27	0.01	0.09	2.64	1.16
$\tilde{V}$	0.37	0.30	0.33	0.33	–	–	–	1.62	0.60	0.01	0.10	0.18	0.12

Table 6 Costa Individual fits (**TBx**)

	C0	bff	bss	bnn	bfs	bfn	bsn	MSE_f	MSE_p	R_f^2	R_p^2	AIC_f	AIC_p
D1	2.06	2.03	0.99	0.90	–	–	–	0.42	0.12	0.84	0.96	9.73	12.30
D2	2.14	2.37	1.49	1.36	–	–	–	0.15	0.12	0.98	0.99	11.77	12.24
D3	2.47	2.28	1.34	1.22	–	–	–	0.12	0.09	0.99	0.99	12.27	12.82
D4	2.56	1.98	1.72	1.57	–	–	–	0.21	0.16	0.99	0.99	11.12	11.72
D5	2.00	3.36	1.19	1.08	–	-	–	0.20	0.22	0.96	0.97	11.21	11.04
D6	3.61	2.45	1.01	0.92	–	–	–	0.25	0.22	0.98	0.98	10.80	11.05
D7	5.16	2.11	0.48	0.43	–	–	–	0.88	0.93	0.92	0.92	8.26	8.15
D8	2.17	3.05	0.91	0.83	–	–	–	0.19	0.20	0.95	0.97	11.36	11.19
D9	2.58	2.38	1.24	1.13	–	–	–	0.10	0.08	0.99	0.99	12.68	13.16
D10	1.24	3.21	2.15	1.96	–	–	–	0.60	0.40	0.95	0.98	9.01	9.84
Mean	2.60	2.52	1.25	1.14	–	–	–	0.31	0.25	0.96	0.97	10.82	11.35
SD	1.08	0.50	0.46	0.42	–	–	–	0.25	0.26	0.05	0.02	1.41	1.49
$\tilde{V}$	0.42	0.20	0.37	0.37	–	–	–	0.81	1.01	0.05	0.02	0.13	0.13

Table 7 Costa Individual fits (**STS**)

	C0	bff	bss	bnn	bfs	bfn	bsn	MSE_f	MSE_p	R_f^2	R_p^2	AIC_f	AIC_p
D1	3.86	6.44	4.17	1.84	1.06	0.23	1.29	0.30	10827.82	0.90	0.010	16.41	-4.58
D2	3.86	6.44	4.17	1.84	1.06	0.23	1.29	0.30	11034.17	0.90	0.011	16.41	-4.62
D3	3.24	8.59	3.65	1.20	1.12	1.02	1.85	0.04	17457.16	0.99	0.003	20.69	-5.54
D4	3.24	8.59	3.65	1.20	1.12	1.02	1.85	0.04	19237.76	0.99	0.011	20.69	-5.73
D5	2.47	4.62	3.47	0.23	2.80	2.13	1.64	0.10	208.51	0.98	0.011	18.51	3.32
D6	2.47	4.62	3.47	0.23	2.80	2.13	1.64	0.10	199.52	0.98	0.013	18.51	3.41
D7	0.95	5.77	0.28	0.27	6.27	5.28	5.22	0.74	1.94	0.95	0.018	14.61	12.68
D8	0.95	5.77	0.28	0.27	6.27	5.28	5.22	0.74	1.83	0.95	0.003	14.61	12.79
D9	3.67	5.20	2.65	0.85	1.61	1.35	1.64	0.02	752.77	0.98	0.001	21.46	0.75
D10	3.67	5.20	2.65	0.85	1.61	1.35	1.64	0.02	660.60	0.98	0.009	21.46	1.01
Mean	2.84	6.12	2.85	0.88	2.57	2.00	2.33	0.24	6038.21	0.96	0.01	18.34	1.35
SD	1.12	1.45	1.45	0.64	2.06	1.84	1.53	0.28	7819.67	0.03	0.005	2.70	6.96
$\tilde{V}$	0.39	0.24	0.51	0.73	0.80	0.92	0.66	1.17	1.30	0.04	0.581	0.15	5.16

Table 8 Costa Individual fits (**CMB1: EBx + STS**)

	C0	bff	bss	bnn	bfs	bfn	bsn	MSE_f	MSE_p	R_f^2	R_p^2	AIC_f	AIC_p
D1	1.39	2.27	2.16	0.88	4.52	1.68	3.92	0.40	0.38	0.95	0.87	15.86	15.94
D2	0.93	3.01	2.82	1.37	5.42	2.22	4.79	0.39	0.52	0.97	0.95	15.87	15.32
D3	1.58	3.32	1.33	1.26	3.45	2.23	3.49	0.81	0.44	0.94	0.95	14.41	15.66
D4	1.85	2.89	1.60	1.52	3.04	1.88	3.07	1.15	1.14	0.92	0.95	13.72	13.73
D5	1.55	2.99	2.85	0.37	4.30	3.06	2.43	0.34	0.45	0.95	0.91	16.18	15.61
D6	1.95	2.80	2.67	0.41	3.77	2.61	2.04	0.34	0.46	0.97	0.97	16.15	15.57
D7	1.08	5.09	0.80	0.77	5.87	4.93	4.73	0.78	0.91	0.96	0.77	14.51	14.19
D8	1.01	4.45	1.16	1.11	6.04	5.12	4.81	0.60	0.27	0.96	0.95	15.01	16.65
D9	2.01	2.70	1.67	0.95	3.37	2.35	2.83	0.25	0.19	0.97	0.99	16.74	17.36
D10	1.89	3.08	1.91	1.26	3.42	2.37	2.88	0.52	0.91	0.95	0.92	15.29	14.19
Mean	1.52	3.26	1.90	0.99	4.32	2.85	3.50	0.56	0.57	0.95	0.92	15.37	15.42
SD	0.41	0.85	0.72	0.39	1.11	1.21	1.02	0.28	0.31	0.01	0.06	0.95	1.13
$\tilde{V}$	0.27	0.26	0.38	0.39	0.26	0.42	0.29	0.50	0.55	0.02	0.07	0.06	0.07

Table 9 Costa Individual fits (**CMB2: TBx + STS**)

	C0	bff	bss	bnn	bfs	bfn	bsn	MSE_f	MSE_p	R_f^2	R_p^2	AIC_f	AIC_p
D1	1.59	2.36	1.13	1.08	4.23	1.43	3.73	0.43	0.10	0.90	0.96	15.69	18.71
D2	1.86	2.61	1.55	1.47	3.76	1.10	3.26	0.33	0.08	0.96	0.99	16.19	19.12
D3	2.35	2.54	1.28	1.22	2.63	1.59	2.65	0.55	0.10	0.95	0.99	15.19	18.62
D4	2.56	2.21	1.59	1.51	2.39	1.38	2.39	0.71	0.30	0.95	0.99	14.68	16.40
D5	1.92	3.33	1.44	0.93	3.88	2.48	2.00	0.27	0.27	0.92	0.97	16.64	16.63
D6	2.91	2.59	1.48	0.81	3.01	1.81	1.41	0.27	0.20	0.94	0.98	16.63	17.25
D7	3.33	2.81	0.61	0.58	3.18	2.52	2.30	0.73	0.65	0.90	0.93	14.63	14.86
D8	1.73	3.46	1.00	0.95	4.65	3.83	3.52	0.47	0.14	0.93	0.98	15.52	17.94
D9	2.57	2.49	1.18	1.12	2.93	1.88	2.37	0.19	0.08	0.97	0.99	17.37	19.02
D10	1.51	3.25	1.82	1.74	3.98	2.68	3.29	0.38	0.40	0.96	0.98	15.92	15.83
Mean	2.23	2.76	1.31	1.14	3.46	2.07	2.69	0.43	0.23	0.94	0.98	15.85	17.44
SD	0.61	0.43	0.35	0.35	0.74	0.82	0.74	0.19	0.18	0.02	0.02	0.89	1.47
$\bar{V}$	0.27	0.16	0.27	0.31	0.21	0.40	0.27	0.43	0.79	0.03	0.02	0.06	0.08

A.2 HO model complete results

See Tables 10, 11, 12, 13, 14

Table 10 H O Individual fits (**EBx**)

	a	b	aff	bff	ass	bss	afs	bfs	MSE_f	MSE_p	R_f^2	R_p^2	AIC_f	AIC_p
D1	0.91	3.42	0.55	7.67	2.85	1.72	–	–	0.01	0.74	1.00	0.73	20.43	12.60
D2	1.51	4.31	0.92	6.26	1.69	0.33	–	–	0.01	0.24	1.00	0.98	21.20	14.87
D3	1.36	4.35	1.22	5.47	1.79	0.27	–	–	0.00	0.23	1.00	0.98	22.78	14.93
D4	1.98	4.60	0.97	1.99	2.19	0.30	–	–	0.01	0.77	1.00	0.95	21.52	12.53
D5	1.21	4.60	2.55	4.93	0.24	2.17	–	–	0.01	0.20	1.00	0.98	21.98	15.24
D6	1.28	4.42	2.21	5.72	2.12	0.29	–	–	0.02	0.18	1.00	0.98	19.84	15.40
D7	0.34	5.75	5.41	3.12	0.39	0.30	–	–	0.01	1.43	1.00	0.68	21.25	11.28
D8	0.80	4.51	1.95	5.95	0.61	0.54	–	–	0.01	0.18	1.00	0.98	20.75	15.48
D9	1.36	4.27	1.61	4.90	1.47	0.44	–	–	0.00	0.16	1.00	0.98	23.53	15.73
D10	2.05	4.53	0.63	8.93	0.25	2.79	–	–	0.05	0.48	1.00	0.97	17.84	13.48
Mean	1.28	4.48	1.80	5.49	1.36	0.92	–	–	0.01	0.46	1.00	0.92	21.11	14.15
SD	0.52	0.56	1.43	2.00	0.93	0.94	–	–	0.01	0.41	0.00	0.11	1.58	1.56
$\bar{V}$	0.40	0.13	0.80	0.36	0.68	1.03	–	–	1.02	0.90	0.00	0.12	0.07	0.11

Table 11 **H O** Individual fits (**TBx**)

	a	b	aff	bff	ass	bss	afs	bfs	MSE_f	MSE_p	R_f^2	R_p^2	AIC_f	AIC_p
D1	1.09	3.69	1.48	3.33	0.31	0.23	–	–	0.36	0.14	0.79	0.94	14.03	15.95
D2	2.41	3.37	0.79	7.37	0.23	0.25	–	–	0.14	0.09	1.00	0.99	15.96	16.89
D3	2.55	3.11	0.98	6.77	0.23	0.26	–	–	0.10	0.07	0.99	0.98	16.54	17.43
D4	3.31	3.37	0.55	7.26	0.23	0.25	–	–	0.51	0.34	0.98	0.99	13.35	14.16
D5	1.46	4.35	2.94	4.48	0.23	0.25	–	–	0.14	0.16	0.98	0.99	15.97	15.72
D6	2.77	2.91	2.30	5.55	0.23	0.25	–	–	0.10	0.12	0.99	0.99	16.55	16.22
D7	1.71	2.31	3.77	4.01	0.23	0.23	–	–	0.64	0.66	0.94	0.94	12.91	12.84
D8	1.27	3.69	2.51	4.69	0.23	0.25	–	–	0.13	0.15	0.98	0.99	16.05	15.78
D9	2.32	3.27	1.60	5.08	0.23	0.25	–	–	0.08	0.04	0.99	0.99	17.08	18.22
D10	2.03	4.62	0.57	9.81	0.23	0.25	–	–	0.39	0.24	0.98	0.99	13.90	14.86
Mean	2.09	3.47	1.75	5.84	0.24	0.25	–	–	0.26	0.20	0.96	0.98	15.23	15.81
SD	0.71	0.67	1.10	1.96	0.02	0.01	–	–	0.20	0.18	0.06	0.02	1.52	1.57
$\bar{V}$	0.34	0.19	0.63	0.34	0.10	0.03	–	–	0.77	0.91	0.06	0.02	0.10	0.10

Table 12 **H O** Individual fits (**STS**)

	a	b	aff	bff	ass	bss	afs	bfs	MSE_f	MSE_p	R_f^2	R_p^2	AIC_f	AIC_p
D1	0.70	5.90	9.81	9.81	9.78	9.23	1.14	3.33	0.34	2485.61	0.95	0.019	18.15	0.36
D2	0.70	5.90	9.81	9.81	9.78	9.23	1.14	3.33	0.34	2446.81	0.95	0.015	18.15	0.39
D3	1.77	3.89	9.82	9.82	6.24	1.58	0.23	0.24	0.31	1111.85	0.87	0.012	18.35	1.97
D4	1.77	3.89	9.82	9.82	6.24	1.58	0.23	0.24	0.31	1223.45	0.87	0.015	18.35	1.78
D5	2.38	1.75	9.46	8.62	4.27	9.78	0.57	9.77	0.17	843.03	0.93	0.016	19.57	2.53
D6	2.38	1.75	9.46	8.62	4.27	9.78	0.57	9.77	0.17	827.15	0.93	0.010	19.57	2.56
D7	2.26	5.88	9.81	9.81	0.23	0.31	0.51	9.79	0.58	1219.46	0.95	0.004	17.07	1.79
D8	2.26	5.88	9.81	9.81	0.23	0.31	0.51	9.79	0.58	1291.94	0.95	0.014	17.07	1.67
D9	2.63	2.76	9.81	9.81	4.82	8.99	0.39	1.82	0.04	1586.48	0.99	0.012	22.51	1.26
D10	2.63	2.76	9.81	9.81	4.82	8.99	0.39	1.82	0.04	1427.23	0.99	0.005	22.51	1.47
Mean	1.95	4.04	9.74	9.57	5.07	5.98	0.57	4.99	0.29	1446.30	0.94	0.012	19.13	1.58
SD	0.72	1.75	0.15	0.50	3.26	4.36	0.32	4.25	0.19	585.50	0.04	0.005	1.97	0.75
$\bar{V}$	0.37	0.43	0.02	0.05	0.64	0.73	0.57	0.85	0.67	0.40	0.04	0.390	0.10	0.48

Table 13 **H O** Individual fits (**CMB1: EBx + STS**)

	a	b	aff	bff	ass	bss	afs	bfs	MSE_f	MSE_p	R_f^2	R_p^2	AIC_f	AIC_p
D1	1.17	3.44	3.01	0.24	3.16	0.23	1.08	9.10	0.71	2.05	0.84	0.09	16.67	14.56
D2	0.86	5.25	4.33	0.23	4.81	0.23	1.11	8.45	0.96	2.17	0.84	0.77	16.09	14.45
D3	1.95	3.63	5.60	0.23	0.56	0.24	0.69	5.89	1.07	1.32	0.81	0.84	15.86	15.44
D4	1.66	4.58	5.30	0.23	2.27	0.23	0.90	2.70	1.32	2.29	0.79	0.80	15.45	14.34
D5	1.99	3.22	6.67	0.81	1.35	0.24	0.84	9.72	0.93	2.31	0.88	0.81	16.15	14.33
D6	1.96	3.24	7.18	0.72	2.59	0.23	0.79	9.76	0.97	2.52	0.91	0.82	16.05	14.15
D7	3.47	0.74	9.81	0.26	0.23	0.23	1.00	9.82	2.35	6.73	0.64	0.34	14.29	12.19
D8	3.80	1.35	5.66	0.94	0.23	0.23	0.91	9.82	2.31	3.31	0.76	0.20	14.33	13.60
D9	2.76	2.90	4.74	0.24	0.27	0.25	0.55	8.91	0.46	0.97	0.92	0.88	17.54	16.06
D10	2.22	4.16	5.63	0.24	1.64	0.24	0.74	6.44	1.06	3.39	0.91	0.79	15.89	13.56
Mean	2.19	3.25	5.79	0.41	1.71	0.24	0.86	8.06	1.21	2.71	0.83	0.62	15.83	14.27
SD	0.93	1.37	1.83	0.29	1.52	0.01	0.18	2.35	0.63	1.60	0.09	0.34	0.98	1.06
$\bar{V}$	0.43	0.42	0.32	0.70	0.89	0.02	0.20	0.29	0.52	0.59	0.10	0.55	0.06	0.07

Table 14 **H O** Individual fits (**CMB2: TBx + STS**)

	a	b	aff	bff	ass	bss	afs	bfs	MSE_f	MSE_p	R^2_f	R^2_p	AIC_f	AIC_p
D1	1.13	3.71	1.75	2.48	0.23	0.23	1.28	8.72	0.62	0.18	0.75	0.93	16.96	19.47
D2	0.88	5.53	1.44	5.13	2.50	0.23	1.35	8.06	0.52	0.17	0.95	0.99	17.29	19.53
D3	1.99	3.70	2.04	3.78	0.57	0.25	0.70	5.90	0.65	0.13	0.89	0.98	16.87	20.14
D4	1.63	4.89	2.37	1.81	1.98	0.23	1.01	2.36	0.96	0.67	0.89	0.97	16.08	16.80
D5	1.84	3.66	3.30	4.04	0.23	0.24	1.11	8.97	0.32	0.34	0.96	0.97	18.28	18.17
D6	1.96	3.48	3.09	4.44	1.41	0.24	0.99	9.32	0.30	0.22	0.96	0.98	18.44	19.04
D7	2.44	1.57	3.77	3.90	0.23	0.23	1.17	9.81	1.62	0.99	0.63	0.90	15.03	16.02
D8	2.01	2.62	2.41	4.72	0.23	0.23	1.19	9.79	1.46	0.34	0.93	0.93	15.24	18.15
D9	2.63	3.00	1.79	4.53	0.23	0.24	0.74	8.15	0.23	0.10	0.93	0.99	18.98	20.55
D10	2.22	4.31	0.63	9.65	0.23	0.25	0.99	6.33	0.34	0.26	0.92	0.99	18.13	18.72
Mean	1.87	3.65	2.26	4.45	0.78	0.24	1.05	7.74	0.70	0.34	0.88	0.96	17.13	18.66
SD	0.54	1.12	0.94	2.09	0.86	0.01	0.21	2.31	0.49	0.28	0.11	0.03	1.36	1.42
$\bar{V}$	0.29	0.31	0.42	0.47	1.09	0.03	0.20	0.30	0.70	0.83	0.12	0.03	0.08	0.08

A.3 HOE model complete results

See Tables 15, 16, 17, 18, 19.

Table 15 **HOE** Individual fits (**EBx**)

	a	b	aff	bff	ass	bss	afs	bfs	afn	bfn	asn	bsn	MSE_f	MSE_p	R^2_f	R^2_p	AIC_f	AIC_p
D1	0.78	3.63	0.55	7.67	2.95	1.95	–	–	–	–	–	–	0.01	0.74	1.00	0.73	20.42	12.60
D2	1.51	4.31	0.92	6.26	1.69	0.31	–	–	–	–	–	–	0.01	0.24	1.00	0.98	21.20	14.88
D3	1.34	4.36	1.22	5.47	1.80	0.37	–	–	–	–	–	–	0.00	0.23	1.00	0.98	22.76	14.92
D4	1.98	4.60	0.97	1.99	2.19	0.30	–	–	–	–	–	–	0.01	0.77	1.00	0.95	21.52	12.53
D5	1.22	4.58	2.55	4.93	0.24	1.53	–	–	–	–	–	–	0.01	0.20	1.00	0.98	21.97	15.24
D6	1.28	4.43	2.21	5.72	2.12	0.29	–	–	–	–	–	–	0.02	0.18	1.00	0.98	19.84	15.40
D7	0.34	5.75	5.41	3.12	0.39	0.30	–	–	–	–	–	–	0.01	1.43	1.00	0.68	21.25	11.28
D8	0.80	4.52	1.95	5.95	0.61	0.61	–	–	–	–	–	–	0.01	0.18	1.00	0.98	20.75	15.48
D9	1.36	4.27	1.61	4.90	1.47	0.44	–	–	–	–	–	–	0.00	0.16	1.00	0.98	23.53	15.73
D10	2.04	4.53	0.63	8.93	0.25	3.16	–	–	–	–	–	–	0.05	0.48	1.00	0.97	17.84	13.47
Mean	1.26	4.50	1.80	5.49	1.37	0.93	–	–	–	–	–	–	0.01	0.46	1.00	0.92	21.11	14.15
SD	0.53	0.52	1.43	2.00	0.95	0.98	–	–	–	–	–	–	0.01	0.41	0.00	0.11	1.58	1.56
$\bar{V}$	0.42	0.12	0.80	0.36	0.69	1.06	–	–	–	–	–	–	1.02	0.90	0.00	0.12	0.07	0.11

Table 16 **HOE** Individual fits (**TBx**)

	a	b	aff	bff	ass	bss	afs	bfs	afn	bfn	asn	bsn	MSE_f	MSE_p	R_f^2	R_p^2	AIC_f	AIC_p
D1	1.09	3.69	1.48	3.33	0.31	0.23	-	–	–	–	–	–	0.36	0.14	0.79	0.94	14.03	15.95
D2	2.42	3.37	0.79	7.37	0.23	0.25	-	–	–	–	–	–	0.14	0.09	1.00	0.99	15.96	16.89
D3	2.55	3.11	0.98	6.77	0.23	0.25	-	–	–	–	–	–	0.10	0.07	0.99	0.98	16.54	17.43
D4	3.31	3.37	0.55	7.26	0.23	0.25	-	–	–	–	–	–	0.51	0.34	0.98	0.99	13.35	14.16
D5	1.45	4.35	2.94	4.48	0.23	0.31	-	–	–	–	–	–	0.14	0.16	0.98	0.99	15.97	15.72
D6	2.77	2.91	2.30	5.55	0.23	0.25	-	–	–	–	–	–	0.10	0.12	0.99	0.99	16.55	16.22
D7	1.71	2.31	3.77	4.01	0.23	0.24	-	–	–	–	–	–	0.64	0.66	0.94	0.94	12.91	12.84
D8	1.27	3.69	2.51	4.69	0.23	0.25	-	–	–	–	–	–	0.13	0.15	0.98	0.99	16.05	15.78
D9	2.32	3.27	1.60	5.08	0.23	0.25	-	–	–	–	–	–	0.08	0.04	0.99	0.99	17.08	18.22
D10	2.03	4.62	0.57	9.82	0.23	0.23	-	–	–	–	–	–	0.39	0.24	0.98	0.99	13.90	14.86
Mean	2.09	3.47	1.75	5.84	0.24	0.25	-	–	–	–	–	–	0.26	0.20	0.96	0.98	15.23	15.81
SD	0.71	0.67	1.10	1.96	0.03	0.02	-	–	–	–	–	–	0.20	0.18	0.06	0.02	1.52	1.57
$\bar{V}$	0.34	0.19	0.63	0.34	0.10	0.08	-	–	–	–	–	–	0.77	0.91	0.06	0.02	0.10	0.10

Table 17 **HOE** Individual fits (**STS**)

	a	b	aff	bff	ass	bss	afs	bfs	afn	bfn	asn	bsn	MSE_f	MSE_p	R_f^2	R_p^2	AIC_f	AIC_p
D1	0.24	2.70	9.81	8.14	3.75	9.73	1.48	6.67	0.44	7.04	1.35	7.13	0.22	748.85	0.94	0.011	27.04	10.76
D2	0.24	2.70	9.81	8.14	3.75	9.73	1.48	6.67	0.44	7.04	1.35	7.13	0.22	701.94	0.94	0.008	27.04	10.89
D3	0.32	7.50	9.82	9.82	3.05	8.33	2.48	1.01	7.69	5.27	0.32	5.34	0.22	1216.94	0.97	0.007	27.04	9.79
D4	0.32	7.50	9.82	9.82	3.05	8.33	2.48	1.01	7.69	5.27	0.32	5.34	0.22	1332.55	0.97	0.017	27.04	9.61
D5	2.38	1.03	8.32	9.13	4.85	9.78	0.78	8.76	0.24	9.55	0.29	0.29	0.11	888.81	0.98	0.019	28.33	10.42
D6	2.38	1.03	8.32	9.13	4.85	9.78	0.78	8.76	0.24	9.55	0.29	0.29	0.11	872.76	0.98	0.013	28.33	10.46
D7	2.02	3.61	9.81	9.81	0.23	0.31	0.95	9.78	0.39	8.08	0.44	9.64	0.56	1020.76	0.95	0.017	25.15	10.14
D8	2.02	3.61	9.81	9.81	0.23	0.31	0.95	9.78	0.39	8.08	0.44	9.64	0.56	1087.70	0.95	0.018	25.15	10.02
D9	0.25	9.32	9.80	9.79	3.78	9.39	3.38	0.53	5.85	1.34	1.35	1.16	0.03	1503.09	0.99	0.001	30.97	9.37
D10	0.25	9.32	9.80	9.79	3.78	9.39	3.38	0.53	5.85	1.34	1.35	1.16	0.03	1343.79	0.99	0.011	30.97	9.59
Mean	1.04	4.83	9.51	9.34	3.14	7.51	1.82	5.35	2.92	6.26	0.75	4.71	0.23	1071.72	0.96	0.012	27.70	10.11
SD	1.01	3.26	0.63	0.69	1.65	3.83	1.04	4.08	3.37	2.98	0.52	3.73	0.19	272.05	0.02	0.006	2.02	0.52
$\bar{V}$	0.97	0.67	0.07	0.07	0.53	0.51	0.57	0.76	1.15	0.48	0.69	0.79	0.83	0.25	0.02	0.473	0.07	0.05

Table 18 **HOE** Individual fits (**CMB1: EBx + STS**)

	a	b	aff	bff	ass	bss	afs	bfs	afn	bfn	asn	bsn	MSE_f	MSE_p	R_f^2	R_p^2	AIC_f	AIC_p
D1	0.44	4.89	3.50	0.23	2.60	2.42	1.63	7.82	0.24	9.32	1.26	7.71	0.41	1.63	0.97	0.32	25.80	23.02
D2	0.38	6.62	5.17	0.23	1.63	4.68	1.75	7.08	0.23	9.72	1.29	7.29	0.52	1.28	0.97	0.84	25.30	23.50
D3	0.24	7.13	6.35	0.23	1.20	6.16	2.60	3.11	2.90	6.76	0.96	5.78	0.96	1.56	0.92	0.78	24.09	23.11
D4	0.24	7.42	6.11	0.23	1.08	8.46	2.64	2.99	3.03	6.74	0.94	5.70	1.35	2.89	0.89	0.76	23.40	21.88
D5	0.23	7.79	6.70	0.83	3.80	0.24	3.82	3.46	3.11	6.10	9.78	0.67	0.63	2.11	0.94	0.80	24.93	22.51
D6	0.23	7.80	7.13	0.77	4.93	0.34	3.76	3.32	3.41	6.30	9.78	0.63	0.67	2.28	0.95	0.79	24.81	22.35
D7	0.32	5.93	9.27	0.77	0.23	0.30	2.49	7.09	1.66	6.91	2.33	5.84	0.71	3.38	0.96	0.38	24.68	21.56
D8	0.74	4.80	5.98	1.19	0.23	0.30	2.14	7.56	1.39	7.38	1.82	6.27	0.89	0.94	0.96	0.88	24.23	24.13
D9	0.23	7.30	5.64	0.23	1.78	4.74	3.33	3.30	3.60	6.48	3.02	2.93	0.37	1.03	0.95	0.87	25.99	23.95
D10	0.23	8.35	6.49	0.23	1.54	6.54	3.43	2.88	4.10	6.38	3.11	2.56	0.81	3.08	0.95	0.80	24.43	21.75
Mean	0.33	6.80	6.23	0.50	1.90	3.42	2.76	4.86	2.37	7.21	3.43	4.54	0.73	2.02	0.95	0.72	24.77	22.78
SD	0.16	1.23	1.47	0.36	1.50	3.09	0.80	2.19	1.39	1.27	3.44	2.62	0.29	0.88	0.03	0.20	0.79	0.91
$\bar{V}$	0.49	0.18	0.24	0.73	0.79	0.90	0.29	0.45	0.59	0.18	1.00	0.58	0.40	0.43	0.03	0.28	0.03	0.04

Table 19 **HOE** Individual fits (**CMB2: TBx + STS**)

	a	b	aff	bff	ass	bss	afs	bfs	afn	bfn	asn	bsn	MSE_f	MSE_p	R_f^2	R_p^2	AIC_f	AIC_p
D1	0.54	5.30	1.89	2.33	1.02	0.23	2.01	6.88	0.23	9.80	1.07	7.80	0.40	0.19	0.95	0.93	25.83	27.29
D2	0.52	6.04	1.63	4.81	1.76	4.51	2.23	6.14	0.23	9.80	0.97	7.54	0.38	0.21	0.97	0.99	25.92	27.15
D3	1.54	4.10	2.20	3.62	0.92	2.19	1.36	3.44	0.23	9.76	0.24	8.47	0.60	0.16	0.95	0.99	25.01	27.73
D4	1.29	5.23	2.64	1.57	1.85	2.28	1.47	1.99	0.23	9.68	0.23	6.61	0.98	0.80	0.93	0.97	24.05	24.45
D5	0.53	5.48	3.40	4.01	0.86	7.22	3.59	4.22	2.03	6.22	9.74	0.71	0.25	0.22	0.94	0.98	26.77	26.99
D6	1.70	3.71	2.91	4.74	1.86	0.25	1.55	7.27	0.27	7.40	0.42	0.31	0.25	0.20	0.94	0.98	26.81	27.20
D7	1.67	2.36	4.19	3.56	0.23	0.25	1.44	9.17	0.85	8.51	0.89	8.49	0.79	0.84	0.95	0.93	24.48	24.35
D8	1.23	3.75	2.94	4.06	0.23	0.26	1.76	8.30	1.12	8.15	1.24	7.24	0.57	0.20	0.97	0.98	25.13	27.24
D9	2.08	3.50	2.35	3.57	0.33	0.29	1.33	5.83	0.23	9.76	0.98	4.57	0.21	0.10	0.97	0.99	27.08	28.54
D10	1.79	4.75	0.87	8.42	0.24	6.01	1.71	4.26	0.23	9.76	6.03	0.87	0.39	0.28	0.95	0.99	25.90	26.55
Mean	1.29	4.42	2.50	4.07	0.93	2.35	1.85	5.75	0.57	8.89	2.18	5.26	0.48	0.32	0.95	0.97	25.70	26.75
SD	0.58	1.13	0.94	1.82	0.69	2.66	0.68	2.26	0.60	1.27	3.15	3.38	0.25	0.27	0.01	0.02	1.02	1.34
$\bar{V}$	0.45	0.25	0.38	0.45	0.74	1.13	0.37	0.39	1.07	0.14	1.44	0.64	0.52	0.83	0.02	0.02	0.04	0.05

A.4 Global sensitivity analysis Sobol indexes results

See Tables 20, 21, 22, 23, 24, 25, 26, 27, 28.

Table 20 **Costa** model first order Sobol indexes (S_i), results are indicated in percentages

	C_0	b_{ff}	b_{ss}	b_{nn}	b_{fs}	b_{fn}	b_{sn}
MFD	7.23	30.72	16.98	0.79	–	–	–
CFD	7.44	16.40	20.13	3.13	-	–	-
FS	11.33	8.74	–	–	50.16	–	–
FN	14.16	12.56	–	–	–	45.97	–
SF	12.16	–	3.16	–	55.78	–	–
SN	14.10	-	6.04	–	-	-	52.51
NF	15.54	–	–	1.07	-	64.73	-
NS	15.17	–	–	0.61	–	–	57.55

Table 21 **Costa** model secondary order Sobol indexes (S_{ij}), results are indicated in percentages

	C_0	b_{ff}	b_{ss}	b_{nn}	b_{fs}	b_{fn}	b_{sn}
MFD	24.73	43.14	30.14	4.46	-	–	–
CFD	22.76	33.68	38.14	12.66	–	–	–
FS	20.59	15.99	–	–	28.08	–	-
FN	21.75	15.94	–	–	–	25.42	–
SF	22.26	–	6.55	–	24.57	–	–
SN	21.64	–	5.77	–	–	–	24.47
NF	21.57	–	–	1.07	–	19.81	–
NS	19.38	–	–	1.55	–	–	20.94

Table 22 Costa model Sobol Total indexes (S_{Ti}), results are indicated in percentages

	C_0	b_{ff}	b_{ss}	b_{nn}	b_{fs}	b_{fn}	b_{sn}
MFD	31.96	73.86	47.12	5.26	–	–	–
CFD	30.20	50.08	58.27	15.80	–	–	–
FS	31.92	24.73	–	–	78.24	–	–
FN	35.91	28.49	–	–	–	71.40	–
SF	34.42	–	9.71	–	80.35	–	–
SN	35.73	–	11.81	–	–	–	76.98
NF	37.11	–	–	2.14	–	84.54	–
NS	34.55	–	–	2.16	–	–	78.49

Table 23 H O model first order Sobol indexes (S_i), results are indicated in percentages

	a	b	a_{ff}	b_{ff}	a_{ss}	b_{ss}	a_{fs}	b_{fs}
MFD	8.30	62.75	0.50	1.16	0.67	2.79	–	–
CFD	7.45	66.78	–	–	0.53	3.00	–	–
FS	6.51	31.39	0.05	0.08	–	–	7.45	32.43
FN	16.65	67.35	0.08	0.01	–	–	–	–
SF	6.87	35.09	–	–	0.01	0.01	6.46	34.89
SN	13.25	66.12	–	–	0.04	0.05	–	–
NF	14.53	64.53	–	–	–	–	–	–
NS	12.63	65.78	–	–	–	–	-	–

Table 24 H O model secondary order Sobol indexes (S_{ij}), results are indicated in percentages

	a	b	a_{ff}	b_{ff}	a_{ss}	b_{ss}	a_{fs}	b_{fs}
MFD	22.01	23.99	0.21	0.26	0.85	1.19	–	–
CFD	22.46	19.16	–	–	1.04	1.04	–	-
FS	10.85	12.28	0.01	0.06	–	–	9.40	10.87
FN	19.34	21.04	0.04	0.05	–	–	–	–
SF	10.27	8.99	–	–	0.05	0.03	10.11	7.96
SN	21.45	21.22	–	–	0.07	0.01	–	–
NF	20.47	22.04	–	–	–	–	–	–
NS	19.98	20.33	–	-	–	–	-	–

Table 25 H O model Sobol Total indexes (S_{Ti}), results are indicated in percentages

	a	b	a_{ff}	b_{ff}	a_{ss}	b_{ss}	a_{fs}	b_{fs}
MFD	30.31	86.73	0.71	1.42	1.52	3.98	-	–
CFD	29.92	85.94	–	–	1.58	4.04	–	–
FS	17.36	43.67	0.05	0.03	–	–	16.85	43.30
FN	35.98	88.39	0.11	0.06	–	–	–	-
SF	17.14	44.08	–	–	0.06	0.03	16.57	42.86
SN	34.70	87.35	–	–	0.11	0.06	–	–
NF	35.00	86.57	–	–	–	–	–	–
NS	32.60	86.11	–	–	–	–	–	–

Table 26 **HOE** model first order Sobol indexes (S_i), results are indicated in percentages

	a	b	a_{ff}	b_{ff}	a_{ss}	b_{ss}	a_{fs}	b_{fs}	a_{fn}	b_{fn}	a_{sn}	b_{sn}
MFD	7.67	65.06	0.36	0.91	0.71	3.20	–	–	-	–	-	–
CFD	7.13	66.15	–	–	0.47	3.08	–	–	–	–	–	–
FS	6.21	33.43	0.09	0.01	–	–	8.28	31.87	–	–	–	–
FN	0.04	0.02	–	–	–	–	–	9.06	3.31	32.05	–	-
SF	6.15	33.77	–	–	0.11	0.07	7.58	34.39	–	–	–	–
SN	0.01	0.03	–	–	–	–	–	34.33	–	–	0.53	7.95
NF	0.01	0.06	–	–	–	–	–	4.95	0.78	–	–	–
NS	0.01	0.01	–	–	–	–	–	27.64	–	-	2.12	9.92

Table 27 **HOE** model secondary order Sobol indexes (S_{ij}), results are indicated in percentages

	a	b	a_{ff}	b_{ff}	a_{ss}	b_{ss}	a_{fs}	b_{fs}	a_{fn}	b_{fn}	a_{sn}	b_{sn}
MFD	20.25	22.57	0.33	0.46	0.78	0.69	–	–	–	–	–	–
CFD	21.73	21.72	–	–	1.01	0.79	–	–	–	–	–	–
FS	10.38	8.83	0.03	0.02	–	–	8.31	10.59	–	–	–	–
FN	0.01	0.11	–	–	–	–	–	70.97	46.22	59.24	-	–
SF	11.10	9.57	–	-	0.05	0.04	10.59	9.72	–	–	–	-
SN	0.02	0.04	–	-	–	-	–	67.95	–	–	32.53	66.49
NF	0.02	0.01	-	–	–	–	–	63.10	19.41	56.05	–	–
NS	0.04	0.08	-	–	-	–	–	78.36	–	–	29.44	65.48

Table 28 **HOE** model Sobol Total indexes (S_{Ti}), results are indicated in percentages

	a	b	a_{ff}	b_{ff}	a_{ss}	b_{ss}	a_{fs}	b_{fs}	a_{fn}	b_{fn}	a_{sn}	b_{sn}
MFD	27.92	87.63	0.69	1.38	1.50	3.89	–	–	-	–	–	–
CFD	28.86	87.87	–	–	1.47	3.87	–	–	–	–	–	–
FS	16.60	42.26	0.05	0.02	–	–	16.59	42.45	–	–	–	–
FN	0.05	0.13	–	–	–	–	–	80.03	49.53	91.29	–	–
SF	17.25	43.33	–	–	0.16	0.11	18.16	44.11	–	–	–	–
SN	0.03	0.07	–	–	–	–	–	102.28	–	–	33.06	74.44
NF	0.03	0.07	–	–	–	–	–	68.05	20.20	66.97	–	–
NS	0.05	0.09	-	–	–	-	–	106.00	–	–	31.57	75.40

References

1. Zile MR, Baicu CF, Gaasch WH (2004) Diastolic heart failure abnormalities in active relaxation and passive stiffness of the left ventricle. New England J Med 350(19):1953–1959. https://doi.org/10.1056/NEJMoa032566
2. Fomovsky GM, Holmes JW (2010) Evolution of scar structure, mechanics, and ventricular function after myocardial infarction in the rat. American J Physiol-Heart Circulat Physiol 298(1):221–228. https://doi.org/10.1152/ajpheart.00495.2009
3. Pinto JG, Fung Y (1973) Mechanical properties of the heart muscle in the passive state. J Biomech 6(6):597–616. https://doi.org/10.1016/0021-9290(73)90017-1

4. Demer LL, Yin F (1983) Passive biaxial mechanical properties of isolated canine myocardium. The J Physiol 339(1):615–630. https://doi.org/10.1113/jphysiol.1983.sp014738
5. Humphrey J, Strumpf R, Yin F (1990a) Determination of a constitutive relation for passive myocardium: I.- a new functional form. J Biomech Eng 112:333–346. https://doi.org/10.1115/1.2891193
6. Humphrey J, Strumpf R, Yin F (1990b) Determination of a constitutive relation for passive myocardium: II.- parameter estimation. J Biomech Eng 112:333–346. https://doi.org/10.1115/1.2891194
7. Novak VP, Yin F, Humphrey J (1994) Regional mechanical properties of passive myocardium. J Biomech 27(4):403–412. https://doi.org/10.1016/0021-9290(94)90016-7
8. Sacks M, Chuong C (1993) Biaxial mechanical properties of passive right ventricular free wall myocardium. J Biomech Eng 115:202–205. https://doi.org/10.1115/1.2894122
9. Ghaemi H, Behdinan K, Spence A (2009) In vitro technique in estimation of passive mechanical properties of bovine heart: part I. experimental techniques and data. Med Eng Phys 31(1):76–82. https://doi.org/10.1016/j.medengphy.2008.04.008
10. Hill MR, Simon MA, Valdez-Jasso D, Zhang W, Champion HC, Sacks MS (2014) Structural and mechanical adaptations of right ventricle free wall myocardium to pressure overload. Annals Biomed Eng 42(12):2451–2465. https://doi.org/10.1007/s10439-014-1096-3
11. Nemavhola F (2021) Study of biaxial mechanical properties of the passive pig heart: material characterisation and categorisation of regional differences. Int J Mech Mater Eng 16(1):1–14. https://doi.org/10.1186/s40712-021-00128-4
12. Ngwangwa H, Nemavhola F, Pandelani T, Msibi M, Mabuda I, Davies N, Franz T (2022) Determination of cross-directional and cross-wall variations of passive biaxial mechanical properties of rat myocardia. Processes 10(4):629. https://doi.org/10.3390/pr10040629
13. Ahmad F, Soe S, Albon J, Errington R, Theobald P (2023) Quantifying the microstructural and biomechanical changes in the porcine ventricles during growth and remodelling. Acta Biomaterialia 171:166–192. https://doi.org/10.1016/j.actbio.2023.09.044
14. Dokos S, Smaill BH, Young AA, LeGrice IJ (2002) Shear properties of passive ventricular myocardium. American J Physiol-Heart Circulat Physiol 283(6):2650–2659. https://doi.org/10.1152/ajpheart.00111.2002
15. Kakaletsis S, Meador WD, Mathur M, Sugerman GP, Jazwiec T, Malinowski M, Lejeune E, Timek TA, Rausch MK (2021) Right ventricular myocardial mechanics: multi-modal deformation, microstructure, modeling, and comparison to the left ventricle. Acta Biomaterialia 123:154–166. https://doi.org/10.1016/j.actbio.2020.12.006
16. Sommer G, Schriefl AJ, Andrä M, Sacherer M, Viertler C, Wolinski H, Holzapfel GA (2015) Biomechanical properties and microstructure of human ventricular myocardium. Acta Biomaterialia 24:172–192. https://doi.org/10.1016/j.actbio.2015.06.031
17. Laita N, Aparici-Gil A, Oliván-Viguera A, Pérez-Martínez A, Martínez MÁ, Doblaré M, Peña E (2024) A comprehensive experimental analysis of the local passive response across the healthy porcine left ventricle. Acta Biomaterialia 187:261–277. https://doi.org/10.1016/j.actbio.2024.08.028
18. Avazmohammadi R, Li DS, Leahy T, Shih E, Soares JS, Gorman JH, Gorman RC, Sacks MS (2018) An integrated inverse model-experimental approach to determine soft tissue three-dimensional constitutive parameters: application to post-infarcted myocardium. Biomechanics and Modeling in Mechanobiology 17(1):31–53. https://doi.org/10.1007/s10237-017-0943-1
19. Li DS, Avazmohammadi R, Merchant SS, Kawamura T, Hsu EW, Gorman JH III, Gorman RC, Sacks MS (2020) Insights into the passive mechanical behavior of left ventricular myocardium using a robust constitutive model based on full 3d kinematics. J Mech Behav Biomed Mater 103:103508. https://doi.org/10.1016/j.jmbbm.2019.103508
20. Augenstein KF, Cowan BR, LeGrice IJ, Nielsen PM, Young AA (2005) Method and apparatus for soft tissue material parameter estimation using tissue tagged magnetic resonance imaging. J Biomech Eng 127(1):148–157. https://doi.org/10.1115/1.1835360
21. Augenstein KF, Cowan BR, LeGrice IJ, Young AA (2006) Estimation of cardiac hyperelastic material properties from mri tissue tagging and diffusion tensor imaging. In: Medical Image Computing and Computer-Assisted Intervention–MICCAI 2006: 9th International Conference, Copenhagen, Denmark, October 1-6, 2006. Proceedings, Part I 9, pp. 628–635 . https://doi.org/10.1007/11866565_77 . Springer Berlin Heidelberg. https://link.springer.com/chapter/10.1007/11866565_77#citeas
22. Wang VY, Lam H, Ennis DB, Cowan BR, Young AA, Nash MP (2009) Modelling passive diastolic mechanics with quantitative mri of cardiac structure and function. Med Image Anal 13(5):773–784. https://doi.org/10.1016/j.media.2009.07.006
23. Xi J, Lamata P, Lee J, Moireau P, Chapelle D, Smith N (2011) Myocardial transversely isotropic material parameter estimation from in-silico measurements based on a reduced-order unscented kalman filter. J Mech Behav Biomed Mater 4(7):1090–1102. https://doi.org/10.1016/j.jmbbm.2011.03.018
24. Gao H, Li W, Cai L, Berry C, Luo X (2015) Parameter estimation in a Holzapfel-Ogden law for healthy myocardium. J Eng Math 95:231–248. https://doi.org/10.1007/s10665-014-9740-3
25. Rumindo GK, Ohayon J, Croisille P, Clarysse P (2020) In vivo estimation of normal left ventricular stiffness and contractility based on routine cine mr acquisition. Med Eng Phys 85:16–26. https://doi.org/10.1016/j.medengphy.2020.09.003
26. Fuchs R, Brinker J, Maughan W, Weisfeldt M, Yin F (1981) Coronary flow limitation during the development of ischemia: effect of atrial pacing in patients with left anterior descending coronary artery disease. American

J Cardiol 48:1029–1036. https://doi.org/10.1016/0002-9149(81)90316-7
27. Guccione JM, McCulloch AD, Waldman LK (1991) Passive material properties of intact ventricular myocardium determined from a cylindrical model. J Biomech Eng 113(1):42–55. https://doi.org/10.1115/1.2894084
28. Humphrey JD, Yin FCP (1987) On constitutive relations and finite deformations of passive cardiac tissue: I. a pseudostrain-energy function. J Biomech Eng 109(4):298–304. https://doi.org/10.1115/1.3138684
29. Yin FC, Strumpf RK, Chew PH, Zeger SL (1987) Quantification of the mechanical properties of noncontracting canine myocardium under simultaneous biaxial loading. J Biomech 20(6):577–589. https://doi.org/10.1016/0021-9290(87)90279-X
30. Lin D, Yin F (1998) A multiaxial constitutive law for mammalian left ventricular myocardium in steady-sate barium contracture of tetanus. J Biomech Eng 120:504–517. https://doi.org/10.1115/1.2798021
31. Kerckhoffs RCP, Bovendeerd PHM, Kotte JCS, Prinzen FW, Smits K, Arts T (2003) Homogeneity of cardiac contraction despite physiological asynchrony of depolarization: a model study. Annals Biomed Eng 31:536–547. https://doi.org/10.1114/1.1566447
32. LeGrice IJ, Smaill B, Chai L, Edgar S, Gavin J, Hunter PJ (1995) Laminar structure of the heart: ventricular myocyte arrangement and connective tissue architecture in the dog. American J Physiol-Heart Circulat Physiol 269(2):571–582. https://doi.org/10.1152/ajpheart.1995.269.2.H571
33. Nash MP, Hunter PJ (2000) Computational mechanics of the heart. J Elasticity 61:113–141. https://doi.org/10.1023/A:1011084330767
34. Schmid H, Nash MP, Young AA, Hunter PJ (2006) Myocardial material parameter estimation-a comparative study for simple shear. J Biomech Eng 128(5):742–750. https://doi.org/10.1115/1.2244576
35. Schmid H, Wang Y, Ashton J, Ehret A, Krittian S, Nash MP, Hunter PJ (2009) Myocardial material parameter estimation: a comparison of invariant based orthotropic constitutive equations. Comput Methods Biomech Biomed Eng 12:283–295. https://doi.org/10.1080/10255840802459420
36. Costa KD, Holmes JW, McCulloch AD (2001) Modelling cardiac mechanical properties in three dimensions. Philosophical Trans Royal Soc London. Series A: Math Phys Eng Sci 359(1783):1233–1250. https://doi.org/10.1098/rsta.2001.0828
37. Holzapfel GA, Ogden RW (2009) On planar biaxial tests for anisotropic nonlinearly elastic solids. A continuum mechanical framework. Math Mech Solids 14(5):474–489. https://doi.org/10.1177/1081286507084411
38. Avazmohammadi R, Soares JS, Li DS, Raut SS, Gorman RC, Sacks MS (2019) A contemporary look at biomechanical models of myocardium. Annual Rev Biomed Eng 21:417–442. https://doi.org/10.1146/annurev-bioeng-062117-121129
39. Nordsletten D, Capilnasiu A, Zhang W, Wittgenstein A, Hadjicharalambous M, Sommer G, Sinkus R, Holzapfel GA (2021) A viscoelastic model for human myocardium. Acta Biomaterialia 135:441–457. https://doi.org/10.1016/j.actbio.2021.08.036
40. Laita N, Rosales RM, Wu M, Claus P, Janssens S, Martínez MÁ, Doblaré M, Peña E (2024) On modeling the in vivo ventricular passive mechanical behavior from in vitro experimental properties in porcine hearts. Comput Struct 292:107241. https://doi.org/10.1016/j.compstruc.2023.107241
41. Laita N, Aparici-Gil A, Oliván-Viguera A, Pérez-Martínez A, Martínez MÁ, Doblaré M, Peña E (2024) A comprehensive experimental analysis of the local passive response across the healthy porcine left ventricle. Zenodo Data set. https://doi.org/10.5281/zenodo.12706383
42. Sobol IM (1993) Sensitivity analysis for non-linear mathematical models. Math Model Comput Exp 1:407–414
43. Saltelli A, Annoni P, Azzini I, Campolongo F, Ratto M, Tarantola S (2010) Variance based sensitivity analysis of model output. Design and estimator for the total sensitivity index. Comput Phys Commun 181(2):259–270. https://doi.org/10.1016/j.cpc.2009.09.018
44. Akaike H (1974) A new look at the statistical model identification. IEEE Trans Automatic Control 19(6):716–723. https://doi.org/10.1109/TAC.1974.1100705
45. Anderson D, Burnham K (2004) Model selection and multi-model inference. Second. NY: Springer-Verlag 63(2020):10. https://doi.org/10.1007/b97636
46. Guan D, Ahmad F, Theobald P, Soe S, Luo X, Gao H (2019) On the aic-based model reduction for the general holzapfel-ogden myocardial constitutive law. Biomech Model Mechanobiol 18:1213–1232. https://doi.org/10.1007/s10237-019-01140-6
47. Martonová D, Alkassar M, Seufert J, Holz D, Duong MT, Reischl B, Friedrich O, Leyendecker S (2021) Passive mechanical properties in healthy and infarcted rat left ventricle characterised via a mixture model. J Mech Behav Biomed Mater 119:104430. https://doi.org/10.1016/j.jmbbm.2021.104430
48. Sommer G, Haspinger DC, Andrä M, Sacherer M, Viertler C, Regitnig P, Holzapfel GA (2015) Quantification of shear deformations and corresponding stresses in the biaxially tested human myocardium. Annals Biomed Eng 43(10):2334–2348. https://doi.org/10.1007/s10439-015-1281-z
49. Buoso S, Joyce T, Kozerke S (2021) Personalising left-ventricular biophysical models of the heart using parametric physics-informed neural networks. Med Image Anal 71:102066. https://doi.org/10.1016/j.media.2021.102066
50. Miller R, Kerfoot E, Mauger C, Ismail TF, Young AA, Nordsletten DA (2021) An implementation of patient-specific biventricular mechanics simulations with a deep learning and computational pipeline. Front Physiol 12:716597. https://doi.org/10.3389/fphys.2021.716597
51. Motiwale S, Zhang W, Feldmeier R, Sacks MS (2024) A neural network finite element approach for high speed cardiac mechanics simulations. Comput Methods Appl Mech Eng 427:117060. https://doi.org/10.1016/j.cma.2024.117060
52. Liu H, Soares JS, Walmsley J, Li DS, Raut S, Avazmohammadi R, Iaizzo P, Palmer M, Gorman JH, Gorman RC et al (2021) The impact of myocardial compressibility

on organ-level simulations of the normal and infarcted heart. Scientif Rep 11(1):1–15. https://doi.org/10.1038/s41598-021-92810-y
53. Janssens K, Kraamer M, Barbarotta L, Bovendeerd PH (2023) Post-infarct evolution of ventricular and myocardial function. Biomech Model Mechanobiol 22(6):1815–1828. https://doi.org/10.1007/s10237-023-01734-1
54. Willems R, Janssens KLPM, Bovendeerd PHM, Verhoosel CV, Sluis O (2024) An isogeometric analysis framework for ventricular cardiac mechanics. Comput Mech 73(3):465–506. https://doi.org/10.1007/s00466-023-02376-x
55. Mendiola EA, Neelakantan S, Xiang Q, Xia S, Zhang J, Serpooshan V, Vanderslice P, Avazmohammadi R (2024) An image-driven micromechanical approach to characterize multiscale remodeling in infarcted myocardium. Acta Biomaterialia 173:109–122. https://doi.org/10.1016/j.actbio.2023.10.027